REACTION PATH APPROACH TO DYNAMICS AT A GAS-SOLID INTERFACE: QUANTUM TUNNELING EFFECTS FOR AN ADATOM ON A NON-RIGID METALLIC SURFACE

Steven E. Wonchoba, Wei-Ping Hu, and Donald G. Truhlar

Department of Chemistry and Supercomputer Institute
University of Minnesota, Minneapolis, MN 55455-0431

1. INTRODUCTION

Chemical reactions occurring on metal surfaces are of great technological importance, especially for catalysis.[1–6] Diffusion of reagents on the surface is a critical step in many such reactions.[1,2,7–9] Surface diffusion is also important in molecular beam epitaxy, chemical vapor deposition, and controlled growth of thin films.[10] Diffusion of hydrogen atoms is particularly interesting from a theoretical point of view because of the large quantum mechanical tunneling contributions to this process.[11–38] Laser-induced thermal desorption, field emission fluctuation, and linear optical diffraction techniques have been used to study hydrogen diffusion on several metals, including Ni, W, Ru, Pt, Rh, and Cu.[39–62] Theoretical studies of these processes can complement the data available from these experiments and can eventually be used to study subsurface and bulk diffusion processes more accurately than may be allowed by current experiments. These subsurface and bulk processes are fundamental for energy storage and fuel cell development, hydrogen embrittlement, and the possibility of subsurface hydrogen in catalysis.

Under a broad range of conditions one can model surface diffusion of adsorbed atoms as a unimolecular chemical reaction in which the chemisorption or physisorption bonds of the adatom at an initial site are broken and new bonds are formed at another site. The system composed of the adatom bound at the initial site is called the reactant, and the system composed of the adatom bound at the final site is called the product.

In Section 2 we provide an overview of the reaction-path approach for calculating rate constants of chemical reactions that involve large tunneling effects. We assume that the nuclear

Theoretical and Computational Approaches to Interface Phenomena
Edited by H.L. Sellers and J.T. Golab, Plenum Press, New York, 1994

motion is governed by an effective potential. Section 2.1 discusses the Born-Oppenheimer-Huang electronic adiabatic approximation for an adatom on a metal, which provides the justification for this assumption. The reaction-path approach involves two steps: variational transition state theory with quantized vibrations for the overbarrier reactive flux, reviewed in section 2.2, and multidimensional semiclassical approximations for tunneling, reviewed in Section 2.3. The semiclassical tunneling method presented here assumes small curvature of the reaction path in isoinertial coordinates, which is a reasonable assumption for processes such as diffusion of hydrogen on metals, although more general tunneling approaches are available for other cases. In section 2.4 we discuss the embedded cluster method which is used to model the hydrogen-metal systems studied with these theoretical dynamical methods.

In section 3, we present recent results of applying these methods to hydrogen and deuterium diffusion on Cu(100) and to hydrogen diffusion on Ni(100).

2. METHODS

2.1. Born-Oppenheimer-Huang Approximation for a Metal

Often the existence of a potential energy function governing the atomic motions in a system to be simulated is taken as a given. But this question merits further thought for systems involving metals.

For molecular and insulating solids, the existence of potential energy functions governing the internuclear (interatomic) motion is usually justified by the perturbational method used by Born and Oppenheimer[63] or the variational method used by Born and Huang.[64] Either method provides a justification for the separation of electronic and nuclear motion in which the electronic motion adjusts adiabatically to the nuclear motions. At this point a comment is in order on the validity of the electronic adiabatic approximation for metals. Perturbation theory shows that the leading nonadiabatic corrections are of the order of the vibrational excitation energies divided by the electronic excitation energies.[65] Let the maximum vibrational frequency in wavenumbers be $\overline{\upsilon}_{\max}$, and let the smallest electronic excitation energy be $\Delta E_{\min}$. Then, denoting Planck's constant by h and the speed of light by c, $hc\overline{\upsilon}_{\max}/\Delta E_{\min}$ might be thought to measure the importance of nonadiabatic effects, and—although this ratio is small for closed-shell molecules, insulators, and semiconductors—it is not small for metals, which are conductors. But it has been argued that it would be more appropriate for many properties of a metal to use $hc\overline{\upsilon}_{\max}/\langle E\rangle$, where $\langle E\rangle$ is the average allowed electronic excitation energy. For most of the conduction band, $\langle E\rangle$ is on the order of $0.5(E_F - E_0)$, where E_F is the Fermi energy, and E_0 is the energy at the bottom of the conduction band, since excitations with smaller excitation energy are typically blocked by the Pauli Exclusion Principle.[65] Using this argument leads to the criterion that the electronic adiabatic approximation is expected to be useful if $2hc\overline{\upsilon}_{\max}/(E_F - E_0)$ is small, and this is typically reasonably well satisfied. Thus properties of

a metal, e.g., cohesive energy and normal modes of vibration, that depend on all the valence electrons, and not just those in orbitals near the Fermi level, should be reasonably well described by an electronically adiabatic treatment,[65] and we will adopt such a procedure here. With this justification, we assume that an effective potential is available (the actual forms used for the potential energy functions are provided in Sections 3.1 and 3.2), and we proceed to consider how the dynamics may be modeled.

2.2. Variational Transition State Theory

The fundamental assumption of classical transition state theory (TST) is that any system that crosses a dynamical bottleneck (DB) will do so only once over the course of its trajectory. This is called the no-recrossing assumption.[66–68] Using this assumption, TST calculates the forward rate as the equilibrium one-way flux through the DB from reactants to products.

In order to calculate the reactive flux in a convenient way, we first transform to isoinertial coordinates. Isoinertial coordinates are ones for which the kinetic energy has the same reduced mass for every square term and there are no cross terms. The simplest example is mass-scaled cartesians,[67] which are similar to the mass-weighted cartesians[69] of infrared spectroscopy (the difference being that mass-scaled cartesians have units of length whereas mass-weighted cartesians have units of mass$^{1/2}$ length). We use mass-scaled cartesians in which all the reduced masses are μ. We then calculate the minimum energy path (MEP) from reactants to products, and we define a reaction coordinate, s, as the distance along this MEP. The MEP begins at the saddle point, at which $s = 0$, and follows the path of steepest descent in isoinertial coordinates towards the reactants (s = negative) and the products (s = positive). The reactants and products are called minimum energy sites (MESs), and we define the value of s at the reactant MES as s^R.

We then define a dividing surface orthogonal to the MEP at each s, such that it separates phase space into a reactant region and a product region. This dividing surface is a generalized transition state, and it will be used as a trial DB. Conventional TST corresponds to calculating the equilibrium one-way flux through the trial DB at $s = 0$, which is the highest energy point on the MEP. In generalized TST, we calculate the equilibrium one-way fluxes for other trial surfaces. First consider the result if the calculation is carried out by classical mechanics, which we denote by subscript C. Then, for temperature T and trial DB at s, the calculated rate constant is[66–68]

$$k_C^{GT}(T,s) = \sigma \frac{k_B T}{h} \frac{Q_C^{GT}(T,s)}{Q_C^R(T)} \exp\left(\frac{-V_{MEP}(s)}{k_B T}\right) \tag{1}$$

where the superscript GT indicates a value corresponding to a generalized transition state, σ is the symmetry factor accounting for the number of equivalent paths from a particular reactant site to products [4 for a hydrogen atom diffusing on a (100) face centered cubic (FCC) surface], k_B

is Boltzmann's constant, $V_{MEP}(s)$ is the potential energy of the system along the MEP at s with zero of energy such that $V_{MEP}\left(s^{R}\right)=0$, and $Q_C^{GT}(T,s)$ and $Q_C^{R}(T)$ are the partition functions of the generalized transition state and reactant species, respectively. Notice that since the generalized transition state corresponds to a definite value of s, it does not include any reaction-coordinate motion. The remaining modes, i.e., those included in $Q_C^{GT}(T,s)$, are called transverse modes. Thus, if N is the number of atoms, the number, F, of degrees of freedom of the reactant is $3N$, but the generalized transition state has $3N-1$ degrees of freedom.

As mentioned above, conventional TST places the DB at the saddle point on the PES, i.e., $s = 0$ in Eq. (1), but this is not usually the best DB because this treatment neglects recrossing, and the no-recrossing assumption is not completely correct. The interpretation of Eq. (1) for a unimolecular reaction is that it represents, for a canonical ensemble at temperature T, the local flux in the reactants to products direction through the dividing surface at s divided by the concentration of reactants. Any trajectory that crosses the DB from the reactant side toward products, even if it started on the product side, whether it ends as reactant or product, and whether or not it returns to the DB again and again, and hence gets counted again, will be counted as part of the forward flux, and the resulting rate constant may thus be overestimated. The goal of canonical variational transition state theory (CVT) is to find the best generalized transition state, i.e., the one that minimizes recrossing, which is the root of all the overcounting. Minimizing Eq. (1) with respect to s would lead to the best possible upper limit to the classical rate constant. However, in a canonical ensemble the rate is dominated by systems with energy close to the minimum required to pass through the DB region. For reactions in the threshold regime, the adiabatic separation of transverse coordinates from s is a good approximation,[71–73] so quantum effects on these modes can be included by quantizing transverse modes with fixed s.[74–76] Doing this and also quantizing the reactant modes (which requires no special justification) yields

$$k^{GT}(T,s)=\sigma\frac{k_BT}{h}\frac{Q^{GT}(T,s)}{Q^{R}(T,s)}\exp\left(\frac{-V_{MEP}(s)}{k_BT}\right) \tag{2}$$

where $Q^{GT}(T,s)$ and $Q^{R}(T,s)$ are now defined as sums over states, in contrast to $Q_C^{GT}(T,s)$ and $Q_C^{R}(T)$, which are phase space integrals. The resulting expression in Eq. (2) is a hybrid rate constant, since all modes except the reaction coordinate have been quantized, but the reaction coordinate motion is still classical In quantizing the partition functions, we assume that the reaction coordinate does not couple with any of the other modes and that the total partition function can be separated into electronic and vibrational factors (for processes at a gas-solid interface, there is no rotation or translation, because all modes that would be rotations or translations for a gas-phase species are actually vibrations due to the presence of the surrounding metallic lattice; see section 2.4 discussing the embedded cluster method).

The CVT estimate of the rate constant is obtained by minimizing the calculated rate constant of Eq. (2) with respect to s. The position, s, along the MEP at which the variationally

optimized dividing surface (the variational transition state) at temperature T is ultimately placed is called $s_*^{\mathrm{CVT}}(T)$, and the CVT rate constant is defined as

$$k^{\mathrm{CVT}}(T) = \sigma \frac{k_B T}{h} \frac{Q^{\mathrm{CVT}}(T)}{Q^{\mathrm{R}}(T)} \exp\left(\frac{-V_{\mathrm{MEP}}^{\mathrm{CVT}}(T)}{k_B T} \right) \tag{3}$$

where superscript CVT denotes values determined at $s_*^{\mathrm{CVT}}(T)$.

In the harmonic approximation,

$$Q^{\mathrm{CVT}}(T) = \prod_{m=1}^{F-1} \left[\sum_{v=0}^{\infty} \exp\left(\frac{-\varepsilon_v^{\mathrm{CVT},m}(T)}{k_{\mathrm{B}} T} \right) \right] \tag{4a}$$

$$= \prod_{m=1}^{F-1} \frac{\exp\left(\frac{-hc\overline{\upsilon}_m^{\mathrm{CVT}}(T)}{2k_{\mathrm{B}} T} \right)}{1 - \exp\left(\frac{-hc\overline{\upsilon}_m^{\mathrm{CVT}}(T)}{k_{\mathrm{B}} T} \right)} \tag{4b}$$

where $\varepsilon_v^{\mathrm{CVT},m}(T)$ is the vibrational energy of level v of CVT mode m at temperature T, and $\overline{\upsilon}_m^{\mathrm{CVT}}(T)$ is the frequency of CVT mode m in wavenumbers. Similarly,

$$Q^{\mathrm{R}}(T) = \prod_{m=1}^{F} \left[\sum_{v=0}^{\infty} \exp\left(\frac{-\varepsilon_v^{\mathrm{R},m}}{k_{\mathrm{B}} T} \right) \right] \tag{5a}$$

$$= \prod_{m=1}^{F} \frac{\exp\left(\frac{-hc\overline{\upsilon}_m^{\mathrm{R}}}{2k_{\mathrm{B}} T} \right)}{1 - \exp\left(\frac{-hc\overline{\upsilon}_m^{\mathrm{R}}}{k_{\mathrm{B}} T} \right)} \tag{5b}$$

where $\varepsilon_v^{\mathrm{R},m}$ is the vibrational energy of level v of reactant mode m with frequency $\overline{\upsilon}_m^{\mathrm{R}}$ in wavenumbers.

2.3 Small-Curvature Tunneling Approximations

The neglect of tunneling in the motion along the reaction path often underestimates the true rate constant, especially at low temperatures for processes in which the reaction coordinate is dominated by hydrogenic motion.[76,77] To account for tunneling along the reaction coordinate, we assume that when tunneling occurs, the system is at a low enough temperature that it passes through the DB in the ground state or in a state where the effective potential has almost the same shape as the ground state.[66,78] Under such conditions the effective potential for tunneling is the vibrationally adiabatic ground-state potential energy curve, defined as

$$V_a^G(s) = V_{MEP}(s) + \varepsilon_{transv}^G(s) \tag{6}$$

where $V_{MEP}(s)$ is the potential energy of the system at s on the MEP, and $\varepsilon_{transv}^G(s)$ is the sum over the zero point energies of all transverse modes at s. The maximum of $V_a^G(s)$ is called V_a^{AG} and is the threshold energy (that energy above which the transmission probability is unity and below which it is zero) when the transverse modes are in the quantal ground state, and the reaction coordinate is classical. For surface processes modeled by the embedded cluster approach (see section 2.4), there are a total of $(N_p + 1)$ moving atoms, where N_p is the number of moving metal atoms and the additional atom is the hydrogen atom. This yields $(3N_p + 2)$ transverse modes, which, as mentioned below Eq. (2), are all vibrational.

To include quantal effects on the reaction coordinate, k^{CVT} in Eq. (3) is multiplied by a ground-state transmission coefficient, $\kappa^{CVT/G}$, which accounts for tunneling along the reaction path. The rate constant including tunneling is given by

$$k^{CVT/G}(T) = \kappa^{CVT/G}(T) k^{CVT}(T). \tag{7}$$

The transmission coefficient is the product of two factors.[78] The first factor is the ratio of the Boltzmann average of the quantum probability for transmission through $V_a^G(s)$ to the Boltzmann average of the classical transmission probability for $V_a^G(s)$. The second factor is the ratio of the Boltzmann average of the classical transmission probability with V_a^{AG} as the threshold energy to that with $V_a^G\left[s = s_*^{CVT}(T)\right]$ as the threshold energy. The product of these factors gives the following expression for the ground-state transmission coefficient at the CVT level:

$$\kappa^{CVT/G}(T) = \frac{\int_{V_a^G\left(s=s^R\right)}^{\infty} dE\, P^G(E) \exp\left(-E/k_B T\right)}{\int_{V_a^G\left[s=s_*^{CVT}(T)\right]}^{\infty} dE \exp\left(-E/k_B T\right)} \tag{8}$$

where the lower limit of the integral in the numerator is approximate for a model in which $V_a^G(s)$ increases monotonically from $s = s^R$ to the barrier top, and where $P^G(E)$ is the quantum transmission probability at energy E for the effective potential. This transmission probability is approximated semiclassically by[79]

$$P^G(E) = 1/\left\{1 + \exp\left[2\theta(E)\right]\right\} \tag{9}$$

where $\theta(E)$ is the magnitude of the imaginary action integral for barrier transmission and depends upon the tunneling approximation used.

Several methods by which $P^{G}(E)$ may be approximated are available.[67,68,78,80–89] For most processes, tunneling is not localized to the DB region, and the tunneling path is significantly shorter than the MEP. The best tunneling path should be chosen in principle as that path which minimizes the imaginary action integral.[84] When the curvature along the reaction path is small, we use a small-curvature tunneling approximation,[76,81,82,86–88] in particular the centrifugal-dominant small-curvature semiclassical adiabatic ground-state (CD-SCSAG) method,[86,88] to estimate this effect. This approximation is abbreviated SCT (small-curvature tunneling) for brevity.

In Eq. (8), the tunneling energies are selected from a continuum. However, in a unimolecular reaction, such as the case when an adatom diffuses across a solid surface between minimum energy sites, the reaction coordinate motion is initially restricted to discrete energy levels in the potential energy well, and each site-to-site hop is more accurately represented as a transition initiating in a discrete energy eigenstate rather than from a continuum energy state. This discretization becomes very important at low temperatures when excited states have small occupancies compared to the ground state. To account for this, when such quantization may be important we replace[23] the integral in Eq. (8) by a sum over discrete energy levels E_v^{R} below V_a^{AG} where the energy levels correspond to exciting the reaction-coordinate mode (F) of the reactant. Then, in Eq. (8), only energies above V_a^{AG} are treated as a continuum, and the ground-state transmission coefficient becomes

$$\kappa^{CVT/QG}(T)=\frac{\sum_{v=0}^{M}\frac{dE_v^{R}}{dv}P^{G}\left(E_v^{R}\right)\exp\left(-E_v^{R}/k_BT\right)+\int_{V_a^{AG}}^{\infty}dE\,P^{G}(E)\exp\left(-E/k_BT\right)}{\int_{V_a^{G}\left[s=s_*^{CVT}(T)\right]}^{\infty}dE\,\exp\left(-E/k_BT\right)} \tag{10}$$

where the Q has been introduced in the superscript to indicate that the reaction coordinate energy levels have been quantized. The upper limit, M, of the summation is the number of excited energy eigenstates, E_v^{R}, of the reaction coordinate motion below V_a^{AG}.

A complication occurs in practice because the nature of the reaction coordinate changes along the reaction path. Near the barrier top and over most of the reaction path, the reaction coordinate is a mostly hydrogenic mode. For H diffusion on Ni(100), for example, $s^{R}\approx -1.5$ Å, and the reaction coordinate is mostly hydrogenic from $s\approx -1.2$ Å to $s\approx 1.2$ Å, and there are two transverse hydrogenic modes. For $s\tilde{<}-1.2$ Å, though, the amount of metal-motion character in the reaction coordinate increases until at $s = s^{R}$, there are three hydrogenic transverse modes, with frequencies $\overline{\upsilon}_1^{R} > \overline{\upsilon}_2^{R} = \overline{\upsilon}_3^{R}$. In the harmonic approximation, a very good approximation to the effective potential along the reaction coordinate in the vicinity of the reactant is

$$V_{eff}(s)=V_a^{G}\left(s=s^{R}\right)+\frac{1}{2}hc\left(\overline{\upsilon}_F^{R}-\overline{\upsilon}_3^{R}\right)+\frac{1}{2}f_3\left(s-s^{R}\right)^2. \tag{11}$$

In Eq. (11), f_3 is the force constant corresponding to $\overline{\upsilon}_3^{\mathrm{R}}$ and is equal to $\mu\left(2\pi c\overline{\upsilon}_3^{\mathrm{R}}\right)^2$, and $\overline{\upsilon}_F^{\mathrm{R}}$ is the frequency in wavenumbers of the reactant normal mode that corresponds to the reaction coordinate, which is the lowest-frequency mode at the reactant MES. The energy levels of the reactant, computed from this potential, are

$$E_v^{\mathrm{R}} = V_{\mathrm{a}}^{\mathrm{G}}\left(s = s^{\mathrm{R}}\right) + \frac{1}{2}hc\overline{\upsilon}_F^{\mathrm{R}} + vhc\overline{\upsilon}_3^{\mathrm{R}}, \quad v = 0, 1, ... \tag{12}$$

Then, from Eq. (12),

$$\frac{\mathrm{d}E_v^{\mathrm{R}}}{\mathrm{d}v} = hc\overline{\upsilon}_3^{\mathrm{R}}. \tag{13}$$

When Eq. (10) is used to calculate the transmission coefficient, the small-curvature tunneling approximation is abbreviated SCTQ. Equation (7) is now replaced by

$$k^{\mathrm{CVT/QG}}(T) = \kappa^{\mathrm{CVT/QG}}(T)k^{\mathrm{CVT}}(T). \tag{14}$$

In the SCTQ and SCT approximations, the imaginary action integral in Eq. (9) is given by[81,82,86,88]

$$\theta(E) = (2\pi/h)\int_{s_0}^{s_1}\mathrm{d}s\,\sqrt{2\mu_{\mathrm{eff}}(s)\left[V_{\mathrm{a}}^{\mathrm{G}}(s) - E\right]} \tag{15}$$

where s_0 and s_1 are the limits of the tunneling path, and μ_{eff} is an effective reduced mass which accounts for reaction-path curvature. The physical interpretation is that the effective reduced mass, μ_{eff}, in Eq. (15) is smaller than the inertial reduced mass, μ, because the tunneling path is shorter than the MEP. The effective reduced mass is calculated as[86,88]

$$\mu_{\mathrm{eff}}(s) = \mu\,\min\left\{\begin{array}{l}\exp\left\{-2a(s) - [a(s)]^2 + (\mathrm{d}t/\mathrm{d}s)^2\right\} \\ 1\end{array}\right. \tag{16}$$

where

$$a = C^{3/2}\left\{\sum_{m=1}^{F-1}[C_m(s)]^2[t_m(s)]^{-4}\right\}^{-1/4}, \tag{17}$$

$$t = C^{1/2}\left\{\sum_{m=1}^{F-1}[C_m(s)]^2[t_m(s)]^{-4}\right\}^{-1/4}, \tag{18}$$

$$C = \left\{ \sum_{m=1}^{F-1} [C_m(s)]^2 \right\}^{1/2}, \tag{19}$$

C_m is the reaction-path curvature component along generalized normal mode m, and $t_m(s)$ is the ground-state concave-side vibrational turning point of mode m.

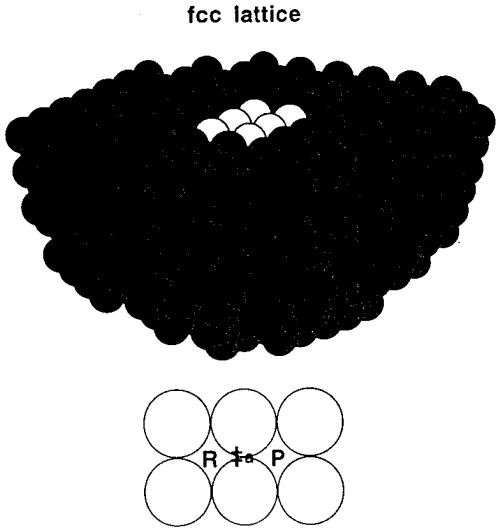

Figure 1. Model of the (100) surface of a face centered cubic (FCC) lattice. The upper figure shows a 6-atom embedded cluster; the lower figure is a close-up looking down on these 6 atoms. R and P are fourfold minimum energy sites for the adatom, and ‡a is a twofold transition state.

For interpretative purposes we note that including only the first term in the numerator of Eq. (10) yields the tunneling rate constant, $k_{tun}(T)$, when substituted in Eq. (14), and including only the second term yields the overbarrier rate constant, $k_{over}(T)$. The fraction of reaction that occurs by tunneling is

$$F_{tun}(T) = \frac{k_{tun}(T)}{k_{tun}(T) + k_{over}(T)}. \tag{20}$$

The diffusion process on an FCC crystal face consists of the hydrogenic atom hopping from an equilibrium four-fold minimum energy binding site, through a two-fold transition state, to another MES. The (100) surface and the stationary points of interest are shown in Figure 1. Assuming that the hops between the MESs are uncorrelated, meaning that the H atom remains at each fourfold site long enough to become thermalized, and therefore the previous history has no effect on each subsequent hop, the surface diffusion coefficient is given by[90]

$$D(T) = \left(\lambda^2/4\right) k_{\text{uni}}(T) \tag{21}$$

where λ is the lateral distance between two MESs (which, for the (100) surface, is equal to $R_0/\sqrt{2}$, where R_0 is the lattice constant), and $k_{\text{uni}}(T)$ is the hopping rate constant.

2.4. Embedded Cluster Method

The hydrogen-metal systems in this study are modeled by the embedded cluster method.[24,29] The systems consist of a single hydrogenic atom and a finite lattice of metal atoms, stacked as (100) FCC planes. A solid-state cluster, consisting of an increasing number of moving atoms (N_p), is surrounded by a set of immovable lattice atoms, fixed at geometries defined by the bulk lattice constant, turning all isolated-molecule rotations and translations into vibrations. We start with N_p = 0, i.e., a rigid metal lattice, and we run the dynamics calculations for this simple (but often unrealistic) system. We then increase N_p, allowing lattice atoms near the representative site of diffusion to move. When these metal atoms are allowed to move, their motion couples to the reaction-coordinate, and this has an effect on the dynamics. As we further increase N_p, and atoms further away from the diffusion site are allowed to move, the coupling to the reaction-coordinate subsides, and the rate constant eventually converges. The movable atoms are chosen as those which fall within the boundaries of either of two hemispheres which have equal radii and are centered at representative sites which depend upon the system being studied. The radii are expanded until the desired number of atoms, N_p, are enclosed within the hemispheres. The centers of the hemispheres are somewhat arbitrary, but need to be well defined for consistency within the study, and they naturally must be near the reactant and product MESs for the specific process; otherwise the coupling of lattice motion to the reaction-coordinate will not converge in a physical manner.

The full lattice is created large enough that all movable atoms in the largest cluster considered (N_{max} = 56 for Cu and N_{max} = 36 for Ni) are surrounded by all interacting neighbors in all directions as far as the distance at which the potential is cut off. The result is that each movable atom is in the environment necessary to be treated as part of an infinite metal lattice.

For the Cu(100) system, the expansion spheres are centered precisely at the reactant and product MESs (as determined by the rigid system with N_p = 0), and the full lattice consists of 324 atoms: 78, 70, 60, 52, 38, and 26 lattice atoms in the first through sixth planes,

descending down perpendicular to the (100) top surface. For the Ni(100) system, which is part of a larger project studying subsurface diffusion, the spheres are centered at octahedral subsurface sites immediately below two adjacent surface atoms. The full lattice consists of 666 atoms: 100, 98, 100, 98, 78, 78, 58, 38, and 18 lattice atoms in the first through ninth planes. These values are somewhat larger than for Cu because the Ni potential energy function has a larger cutoff distance.

Since convergence with respect to N_p was found to be relatively rapid for both systems, we limit the presentation of results and discussion here to the rigid ($N_p = 0$) and fully converged ($N_p = N_{max}$) systems unless otherwise specified. We refer readers to journal articles for some intermediate results.[29,93] The N_p = 56 metal cluster for Cu consists of 20, 18, 16, and 2 moving atoms in the first through fourth planes, and the N_p = 36 metal cluster for Ni consists of 12, 16, and 8 atoms in the first, second, and third planes, respectively. Since there is one adatom, the total number of moving atoms, N, equals $N_p + 1$.

3. APPLICATIONS

We used the POLYRATE[86,94] code to calculate hopping rate constants for H and D on both Cu(100) and Ni(100). We made calculations without tunneling, as well as with SCT and SCTQ tunneling corrections. All vibrational energies are calculated in the harmonic approximation in the present work.

3.1. H/Cu(100) and D/Cu(100)

The potential energy for the H/Cu system is approximated as a sum of pair potentials. As a consequence of the Born-Oppenheimer approximation, these pair potentials are independent of isotopic mass, i.e., the same for D/Cu as for H/Cu. For both the H-Cu and Cu-Cu interaction potential, we used a Morse-spline function of the following form:

$$V(R) = \begin{cases} D_e\left\{\left[1-\exp\left(-\alpha\left(R-R_e\right)\right)\right]^2 - 1\right\}, & R \le R_c - D_c \\ \sum_{i=3}^{5} C_i\left(R - R_c - D_c\right)^i, & R_c - D_c \le R \le R_c + D_c \\ 0, & R > R_c + D_c \end{cases} \qquad (22)$$

where R is the Cu-Cu or H-Cu interatomic distance, D_e, α, and R_e are Morse parameters, and R_c, D_c, and C_i control the spline for smoothing the potential cutoff, $R_c + D_c$. The parameters of the H-Cu potential were based on earlier work by Valone *et al.*[19] and Truong *et al.*[26] For the Cu-Cu interaction,[24–26] D_e and α were chosen[24] to match features of the Lennard-Jones pair

potential of Halicoğlu and Pound,[91] and R_e was chosen[24] to yield an interatomic spacing consistent with the bulk lattice.

For both the Cu-Cu and H-Cu interactions, R_c and the spline width, $2D_c$, were chosen in such a way that the cutoff was smooth and did not introduce any spurious behavior in the frequencies. The parameters C_i were chosen to make the potential function and its first and second derivatives continuous at $R = R_c - D_c$. The values of all pair potential parameters used in Eq. (22) for both the Cu-Cu and H-Cu interactions are listed in Table 1, and the functions are plotted in Figure 2.

Table 1. Potential parameters used for the Cu-Cu and H-Cu interaction in Eq. (22).

Parameter	Cu-Cu	H-Cu
α (Å^{-1})	2.287	1.43
D_e (kcal mol^{-1})	9.4378	7.2875
R_e (Å)	2.578942	2.34
R_c (Å)	5.157883	7.02
C_3 (kcal mol^{-1} Å^{-3})	447.2	154.619
C_4 (kcal mol^{-1} Å^{-4})	6231.8	2168.84
C_5 (kcal mol^{-1} Å^{-5})	23372.7	8156.16
D_c (Å)	0.0529	0.0529

Although this potential energy function is not quantitatively accurate,[29] it has been widely used, and it is qualitatively realistic. Thus it has become a prototype potential to use with new theoretical methods.

The determination of the energetically optimized bulk lattice constant for the assumed potential energy function was a very important process. When lattice atoms move from their original bulk lattice positions defined by the lattice constant, they do so as a result of their proximity to the exposed surface (surface atoms behave differently than bulk atoms because they have different numbers of neighbor atoms) and/or the presence of the adatom. If the lattice constant is not energetically optimized, then when an atom is allowed to move, it will do so not only at the surface but also in the bulk. Therefore, the effect of unfreezing of an atom may not be a result of physical coupling to the process under study but rather a result of inconsistent lattice spacing. As a result, the effect of allowing lattice atoms to move will be overestimated. A lattice constant properly optimized for the potential being used prevents these artifacts.

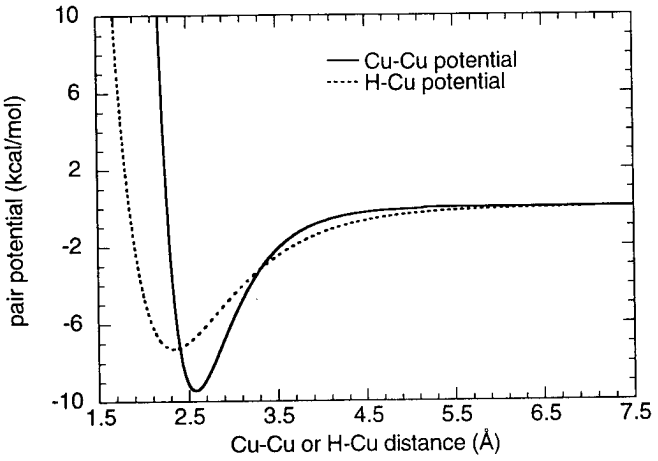

Figure 2. H-Cu and Cu-Cu pair interaction defined by Eq. (22) vs. interatomic distance.

The potential energy of a bulk atom is calculated as one half of the sum of all pair potentials between a selected bulk atom and all other atoms in the system, using the assumed potential energy function for Cu-Cu interaction. The optimum, energetically minimized lattice constant is that which yields the minimum energy for a bulk atom. This value was determined[29] to be 3.5818 Å, which is close to the experimental bulk lattice constant of 3.61 Å.[92] To avoid the artifacts discussed above, the energetically minimized lattice constant was used for all Cu(100) results presented here unless otherwise specified.

Table 2. Binding Energies and barrier heights (kcal/mol) for H on Cu(100).

	Fixed lattice (N_p = 0)	Relaxed lattice (N_p = 56)
Binding Energy		
4-fold site	50.3	50.3
2-fold site	38.4	38.9
Barrier Height		
classical	11.9	11.4
vibrationally adiabatic ground-state	10.6	9.9

Calculated binding energies and barrier heights for H on Cu(100) are given in Table 2. The binding energies are referenced to a hydrogen atom fully separated from the surface, and they do not include zero point contributions. The classical barrier height is calculated as the energy difference between the twofold saddle point and the fourfold reactant MES, and the vibrationally adiabatic ground-state barrier is calculated as the energy difference between V_a^{AG} and $V_a^G(s = s^R)$. Diffusion coefficients for the H/Cu system with the optimized lattice constant are given for a range of temperatures at the CVT (no tunneling), CVT/SCT, and CVT/SCTQ levels for both rigid ($N_p = 0$) and moving ($N_p = 56$) lattices in Table 3. The results for the D/Cu system are given in Table 4.

Table 3. CVT, CVT/SCT, and CVT/SCTQ diffusion coefficients (cm^2/s) for H on Cu(100) surfaces with $N_p = 0$ and $N_p = 56$ at a variety of temperatures. Numbers in parentheses are powers of 10.

	$N_p = 0$			$N_p = 56$		
T (K)	CVT	CVT/SCT	CVT/SCTQ	CVT	CVT/SCT	CVT/SCTQ
40	2.55(-61)	2.00(-23)	4.15(-22)	5.02(-58)	4.49(-22)	1.02(-20)
50	9.27(-50)	3.03(-23)	4.15(-22)	4.03(-47)	6.83(-22)	1.02(-20)
60	4.89(-42)	4.55(-23)	4.15(-22)	7.78(-40)	1.04(-21)	1.03(-20)
80	2.33(-32)	1.16(-22)	4.23(-22)	1.06(-30)	2.84(-21)	1.06(-20)
100	1.57(-26)	4.96(-22)	6.99(-22)	3.42(-25)	1.35(-20)	1.80(-20)
120	1.25(-22)	9.83(-21)	1.01(-20)	1.65(-21)	2.37(-19)	2.25(-19)
200	9.17(-15)	2.18(-14)	9.75(-15)	4.57(-14)	1.53(-13)	1.04(-13)
250	2.25(-12)	3.75(-12)	1.94(-12)	8.37(-12)	1.80(-11)	1.11(-11)
300	9.06(-11)	1.27(-10)	7.63(-11)	2.79(-10)	4.75(-10)	2.92(-10)
400	9.64(-9)	1.16(-8)	8.24(-9)	2.34(-8)	3.16(-8)	2.12(-8)
500	1.64(-7)	1.83(-7)	1.43(-7)	3.45(-7)	4.19(-7)	3.03(-7)
600	1.09(-6)	1.18(-6)	9.72(-7)	2.10(-6)	2.41(-6)	1.86(-6)
800	1.20(-5)	1.25(-5)	1.09(-5)	2.07(-5)	2.23(-5)	1.84(-5)
1000	5.08(-5)	5.23(-5)	4.71(-5)	8.26(-5)	8.68(-5)	7.49(-5)

To evaluate the effect of tunneling on this process, we calculate the ratio of the diffusion coefficients calculated including tunneling to those calculated without tunneling (i.e., CVT/SCT to CVT and CVT/SCTQ to CVT). This quantity is given in Table 5. At high temperatures, tunneling does not contribute significantly to the diffusion coefficient. But as the temperature decreases, tunneling becomes increasingly more important, and at temperatures $\leq$ 100 K, virtually the entire process proceeds by tunneling.

Table 4. CVT, CVT/SCT, and CVT/SCTQ diffusion coefficients (cm^2/s) for D on Cu(100) surfaces with $N_p = 0$ and $N_p = 56$ at a variety of temperatures. Numbers in parentheses are powers of 10.

	$N_p = 0$			$N_p = 56$		
T (K)	CVT	CVT/SCT	CVT/SCTQ	CVT	CVT/SCT	CVT/SCTQ
40	1.92(-63)	4.19(-33)	5.18(-32)	2.34(-60)	2.49(-31)	3.05(-30)
50	1.86(-51)	7.25(-33)	5.20(-32)	5.50(-49)	4.39(-31)	3.06(-30)
60	1.88(-43)	1.55(-32)	5.52(-32)	2.18(-41)	9.78(-31)	3.34(-30)
80	2.02(-33)	9.72(-31)	1.04(-30)	7.28(-32)	6.90(-29)	8.40(-29)
100	2.23(-27)	1.73(-26)	1.78(-26)	3.99(-26)	5.89(-25)	7.91(-25)
120	2.45(-23)	7.76(-23)	6.25(-23)	2.77(-22)	1.50(-21)	2.53(-21)
200	3.43(-15)	4.73(-15)	3.24(-15)	1.56(-14)	2.81(-14)	5.61(-14)
250	1.01(-12)	1.23(-12)	9.11(-13)	3.50(-12)	5.12(-12)	9.65(-12)
300	4.60(-11)	5.24(-11)	4.11(-11)	1.33(-10)	1.73(-10)	3.06(-10)
400	5.58(-9)	6.00(-9)	5.05(-9)	1.30(-8)	1.51(-8)	2.37(-8)
500	1.01(-7)	1.06(-7)	9.27(-8)	2.07(-7)	2.28(-7)	3.32(-7)
600	6.53(-7)	7.25(-7)	6.53(-7)	1.33(-6)	1.42(-6)	1.96(-6)
800	8.02(-6)	8.15(-6)	7.55(-6)	1.37(-5)	1.42(-5)	1.81(-5)
1000	3.48(-5)	3.51(-5)	3.30(-5)	5.60(-5)	5.74(-5)	6.96(-5)

Table 5. Ratio of tunneling to non-tunneling diffusion coefficients for H on a moving ($N_p = 56$) Cu(100) surface. Numbers in parentheses are powers of 10.

T(K)	CVT/SCT / CVT	CVT/SCTQ / CVT
40	8.94(35)	2.03(37)
50	1.69(25)	2.53(26)
60	1.34(18)	1.32(19)
80	2.68(9)	1.00(10)
100	3.95(4)	5.26(4)
120	1.44(2)	1.36(2)
200	3.35	2.28
250	2.15	1.33
300	1.70	1.05
400	1.35	0.91
500	1.21	0.88
600	1.15	0.89
800	1.07	0.89
1000	1.05	0.91

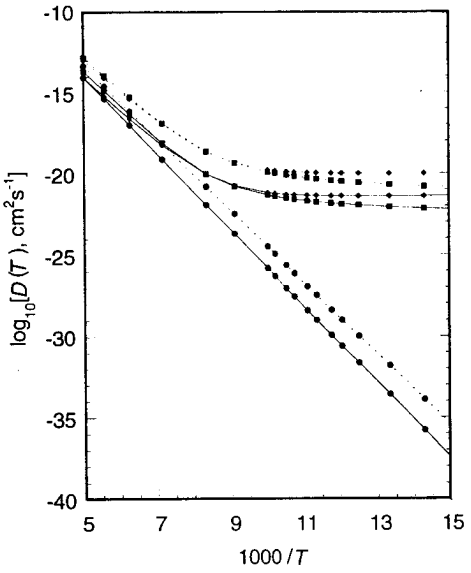

Figure 3. Arrhenius plot for H diffusion on Cu(100) Solid lines are for N_p = 0, dashed lines are for N_p = 56. CVT, CVT/SCT, and CVT/SCTQ diffusion coefficients represented by circles, squares, and diamonds, respectively.

Tables 3 and 4 show that the CVT/SCTQ diffusion coefficient becomes independent of T at very low temperatures. This effect is also shown in the Arrhenius plot of the data in Figure 3. For both rigid and moving surfaces, the plot of the diffusion coefficient with quantized reactant states levels off at approximately 90 K. To quantify the analysis, we next define two temperatures of interest on the Arrhenius plot.

First, we note that the Arrhenius plot of the CVT/SCTQ diffusion coefficients in Figure 3 consists largely of two approximately linear regions (T above approximately 120 K and T below approximately 90 K). An intermediate transition region (T between 90 K and 120 K) of high curvature joins the two linear regions. We define the transition temperature, T_{tr}, as the point of maximum curvature (analytically, the point of maximum second derivative) of this intermediate transition region on the Arrhenius plot.

We will next derive an approximate analytic formula for T_{tr}. We begin by noting that at low temperatures, the denominators of Eqs. (4b) and (5b) closely approach unity, and by using Eqs. (6) and (12) and the convention that $V_{\mathrm{MEP}}\left(s^{\mathrm{R}}\right) = 0$, the ratio of partition functions in Eq.

$$\frac{Q^{\mathrm{CVT}}(T_{\mathrm{low}})}{Q^{\mathrm{R}}(T_{\mathrm{low}})} \approx \exp\left(-\frac{1}{k_{\mathrm{B}}T_{\mathrm{low}}} \left\{ V_{\mathrm{a}}^{\mathrm{G}}\left[s_*^{\mathrm{CVT}}(T_{\mathrm{low}}) \right] - V_{\mathrm{MEP}}^{\mathrm{CVT}}(T_{\mathrm{low}}) - E_0^{\mathrm{R}} \right\} \right) \tag{23}$$

where T_{low} denotes a low temperature.

Next, we approximate the transmission coefficient at low temperature by assuming that only states below $V_{\mathrm{a}}^{\mathrm{AG}}$ make a significant contribution to the diffusion coefficient (i.e., that the contribution due to the states in the energy continuum is negligible). This approximation, along with Eqs. (12) and (13), allows us to write the ground-state transmission coefficient, Eq. (10), as

$$\kappa^{\mathrm{CVT/QG}}(T_{\mathrm{low}}) = \frac{1}{k_{\mathrm{B}}T_{\mathrm{low}}} \exp\left\{ \frac{1}{k_{\mathrm{B}}T_{\mathrm{low}}} V_{\mathrm{a}}^{\mathrm{G}}\left[s_*^{\mathrm{CVT}}(T_{\mathrm{low}}) \right] \right\} hc\overline{\upsilon}_3^{\mathrm{R}} \sum_{v=0}^{M} P^{\mathrm{G}}\left(E_v^{\mathrm{R}}\right) \exp\left(-\frac{E_v^{\mathrm{R}}}{k_{\mathrm{B}}T_{\mathrm{low}}} \right) \tag{24}$$

where the denominator of Eq. (10) has been integrated directly. Substituting Eqs. (12) and (23) into Eq. (3) and then substituting Eqs. (3) and (24) into Eq. (7) gives the following expression for the low-temperature rate constant:

$$k(T_{\mathrm{low}}) = \sigma c\overline{\upsilon}_3^{\mathrm{R}} \sum_{v=0}^{M} P^{\mathrm{G}}\left(E_v^{\mathrm{R}}\right) \exp\left(\frac{-vhc\overline{\upsilon}_3^{\mathrm{R}}}{k_{\mathrm{B}}T_{\mathrm{low}}} \right) \tag{25}$$

and, from Eq. (23),

$$D(T_{\mathrm{low}}) = \frac{\lambda^2}{4} \sigma c\overline{\upsilon}_3^{\mathrm{R}} \sum_{v=0}^{M} P^{\mathrm{G}}\left(E_v^{\mathrm{R}}\right) \exp\left(\frac{-vhc\overline{\upsilon}_3^{\mathrm{R}}}{k_{\mathrm{B}}T_{\mathrm{low}}} \right). \tag{26}$$

For the H/Cu system, in the harmonic approximation of Eq. (12), there are a total of 4 states below $V_{\mathrm{a}}^{\mathrm{AG}}$. Therefore, $M = 3$ in Eqs. (25) and (26). For the D/Cu system, $M = 5$. Equation (25) is also the expression for the tunneling rate constant, $k_{\mathrm{tun}}(T_{\mathrm{low}})$.

Using Eq. (26) as the expression for the low temperature diffusion coefficient, the point of maximum curvature of the Arrhenius plot (Figure 3) occurs when

$$\left. \frac{\mathrm{d}^3\left[D(T_{\mathrm{low}}) \right]}{\mathrm{d}\left(1/T_{\mathrm{low}}\right)^3} \right|_{T_{\mathrm{low}}=T_{\mathrm{tr}}} = 0. \tag{27}$$

Making a parabolic approximation to the vibrationally adiabatic potential energy curve,[95] assuming that E_{a}, the activation energy for the diffusion of the adatom on the surface, is much larger than $hc\overline{\upsilon}_3^{\mathrm{R}}$, and solving for T in Eq. (27) yields the following expression for the transition temperature:[93]

$$T_{\mathrm{tr}} = \frac{hc\left|\overline{\upsilon}^{\ddagger}\right|}{2\pi k_{\mathrm{B}}} \tag{28}$$

where $\left|\overline{\upsilon}^{\ddagger}\right|$ is the magnitude of the imaginary frequency at the top of the potential barrier. Since Eqs. (25) and (26) only differ by a constant, the same result would be obtained if Eq. (25) were used in the third derivative in Eq. (27).

A second temperature of interest on the Arrhenius plot is the point at which the diffusion coefficient levels off and becomes visually temperature independent. At very low temperatures, the $v = 0$ (ground-state) term in Eqs. (25) and (26) dominates the other (excited-state) terms, and the expression for the overall rate constant approaches the low-temperature limit,

$$k(T) \xrightarrow[T\to 0]{} \sigma c \overline{\upsilon}_3^{\mathrm{R}} P^{\mathrm{G}}\left(E_0^{\mathrm{R}}\right) \tag{29}$$

or

$$D(T) \xrightarrow[T\to 0]{} \frac{\lambda^2}{4} \sigma c \overline{\upsilon}_3^{\mathrm{R}} P^{\mathrm{G}}\left(E_0^{\mathrm{R}}\right) \tag{30}$$

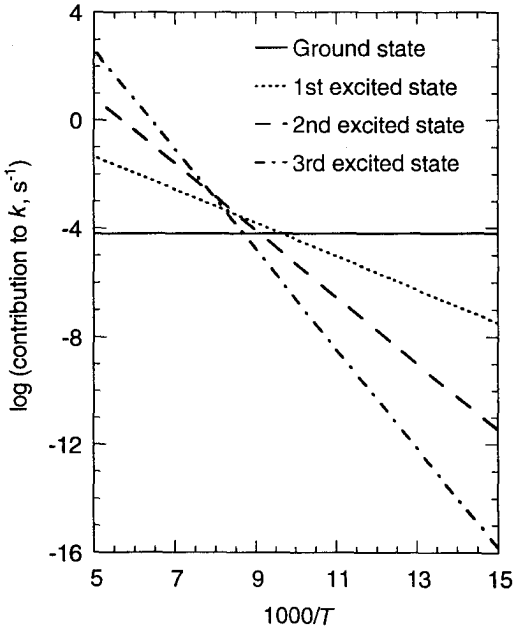

Figure 4. Logarithm to the base 10 of the contribution to the rate constant of each quantized state with energy below $V_{\mathrm{a}}^{\mathrm{AG}}$ versus inverse temperature for H diffusion on Cu(100) with $N_p = 56$.

In Figure 4, the logarithm to the base 10 of the contribution to the overall rate constant of each of the quantized states for the moving ($N_p = 56$) surface is plotted using the same abscissa as was used for the Arrhenius plot in Figure 3. Note that the contribution of the ground state is independent of temperature, and is, in fact, the low-temperature limit to the rate constant given in Eq. (29). At roughly 90 K (the temperature at which the Arrhenius plot levels off), the contribution of the ground state is approximately one order of magnitude greater than the contribution of the first excited state, and it is several orders of magnitude greater than the contributions of the higher excited states (see Figure 4). As a result, we empirically define a level-off temperature, T_0, as the temperature at which the ground-state contribution to the rate constant is greater than the first excited state contribution by one order of magnitude. Making the same approximations that led to Eq. (28) then gives the following expression for the level-off temperature:

$$T_0 = \frac{hc\overline{\upsilon}_3^{\mathrm{R}}}{k_{\mathrm{B}}\left[2\pi\left(\frac{\overline{\upsilon}_3^{\mathrm{R}}}{\left|\overline{\upsilon}^{\ddagger}\right|}\right)+\ln(10)\right]}. \tag{31}$$

The precise values of the transition temperature and the level-off temperature are dependent upon their definitions. However, the definitions given above are reasonable. It can be shown[93] that when the $V_{\mathrm{a}}^{\mathrm{G}}$ is parabolic [which is a reasonably valid approximation[93,95] and was used to derive Eqs. (28) and (31)], then the transition temperature, Eq. (28), corresponds to the temperature at which all states contribute to the rate constant equally. For H on Cu(100) with $N_p = 56$, $\overline{\upsilon}_3^{\mathrm{R}} = 983$ cm^{-1}. Using coordinates scaled to a mass μ of 1 amu, we fit the $V_{\mathrm{a}}^{\mathrm{G}}$ curve to a parabola from $s = -1.3$ Å to $s = 1.3$ Å, where $s^{\mathrm{R}} \approx -1.7$ Å, and we determined the magnitude of the imaginary frequency, $\left|\overline{\upsilon}^{\ddagger}\right|$, from the second derivative of this curve, i.e.,

$$\left|\overline{\upsilon}^{\ddagger}\right| = \frac{1}{2\pi c}\left[\frac{\mathrm{d}^2 V_{\mathrm{a}}^{\mathrm{G}}(s)}{\mathrm{d}s^2}\Big/\mu\right]^{1/2}. \tag{32}$$

This yields $\left|\overline{\upsilon}^{\ddagger}\right| = 458$ cm^{-1}. Then, Eqs. (28) and (31) yield $T_{\mathrm{tr}} = 105$ K and $T_0 = 90$ K, both of which are visually consistent with the Arrhenius plot in Figure 3, indicating that the assumptions made in the derivations are valid.

We note that computing $\left|\overline{\upsilon}^{\ddagger}\right|$ from the second derivative of $V_{\mathrm{MEP}}(s)$ at its maximum instead of from a global fit to $V_{\mathrm{a}}^{\mathrm{G}}(s)$ would have yielded 461 cm^{-1}, resulting in about the same level of agreement.

We can also make comparisons to previous results obtained with other theoretical methods, in particular to the calculations of Sun and Voth[37], who used path integral transition state theory (PI-TST) and to those of Valone, Voter, and Doll[19], who used transition state theory with quantum effective potentials (TST-QEP). We note that these comparisons suffer

from some serious limitations. First, previous work[29] has suggested that the embedded clusters of lattice atoms used in the PI-TST and TST-QEP studies were too small to yield converged rate constants. Second, both studies used the experimental lattice constant, rather than the one energetically optimized one for the assumed potential energy function, to create the Cu lattices. The effects of this have been discussed earlier. Third, the previous studies were limited to a smaller range of temperatures. Despite these limitations, the comparisons are interesting.

In Table 6, the present calculated diffusion coefficients are compared to PI-TST and TST-QEP results. All values listed in this table were calculated using a specially constructed lattice with the experimental lattice constant, R_0 = 3.61 Å, to duplicate the system used in the PI-TST and TST-QEP calculations. In general, the agreement is very good for temperatures greater than or equal to 120 K, but as the temperature is lowered below this, the CVT/SCQT results predict a faster onset of the temperature independence of the diffusion coefficient than do the PI-TST and TST-QEP results. Table 6 also gives the ratios of the diffusion coefficients calculated for a moving surface to those calculated for a rigid surface. The number of moving lattice atoms, N_{moving}, is 56 for the CVT/SCTQ results, 30 for the PI-TST results, and 36 (all surface layer atoms) for the TST-QEP results. These values are also in good agreement for temperatures greater than or equal to 120 K, and the disagreement of the T = 100 K results can be traced to the faster onset of temperature independence seen in the CVT/SCTQ results.

Table 6. Comparisons of CVT/SCT and CVT/SCQT results to PI-TST results.[37] and TST-QEP results.[19] The CVT results in this table were calculated using the experimental lattice constant of 3.61 Å to get a better comparison between the two methods. The number of atoms in the moving lattice, N_{moving}, is 56 for the CVT results, 30 for the PI-TST results, and 36 (all surface atoms) for the TST-QEP results. Numbers in parentheses are powers of 10.

	T(K)	CVT/SCT	CVT/SCQT	PI-TST	TST-QEP
$D(N_p = 0)$	100	2.2(-23)	3.2(-23)	1.2(-24)	3.5(-25)
	120	4.8(-22)	5.2(-22)	3.1(-22)	...
	200	3.3(-15)	4.3(-15)	6.9(-15)	1.0(-14)
	300	3.3(-11)	3.7(-11)	6.9(-11)	7.9(-11)
$D(N_{moving})/D(N_p = 0)$	100	17	8.0	42	7.4
	120	21	18	18	...
	200	7.7	3.0	5.5	2.4
	300	4.1	2.3	3.3	1.9

We now consider the results obtained using the energetically minimized lattice constant. The onset of temperature independence can be seen in the CVT/SCTQ results shown in Figure 3. Figure 5 shows the logarithm to the base 10 of the diffusion coefficient ratio described above. The ratios are plotted for the CVT, CVT/SCT, and CVT/SCTQ levels of theory and

compared to the PI-TST and TST-QEP results which are given in Table 6. The CVT ratios logarithmically increase with decreasing temperature, and the CVT/SCT and CVT/SCQT ratios level off at approximately 110 K. The PI-TST and TST-QEP ratios, however, do not level off, and this may be a consequence of the use of the non-energetically optimized lattice constant in the latter studies (see previous discussion). Finally, we again stress that all of these comparisons must be interpreted with the disclaimers discussed above. For more extensive comparisons of CVT/SCT, PI-TST, and TST-QEP results, we refer readers to Ref. 29.

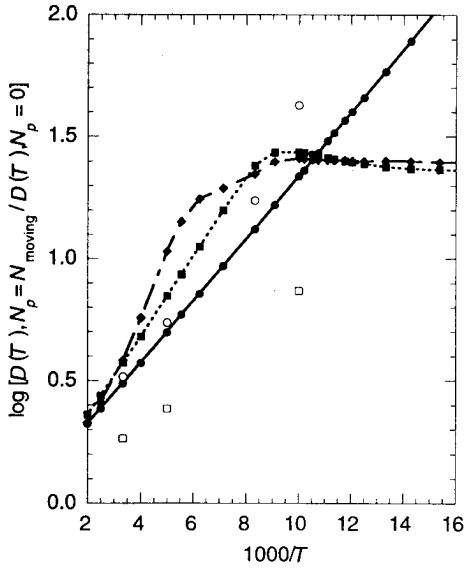

Figure 5. Logarithm to the base 10 of the ratio of diffusion coefficients for H on moving Cu(100) to those for H on rigid Cu(100). CVT, CVT/SCT, and CVT/SCTQ are represented by solid circles, squares, and diamonds, respectively. PI-TST and TST-QEP results are represented by hollow circles and squares, respectively. N_{moving} = 56 for CVT results, 30 for PI-TST results, and 36 (all surface atoms) for TST-QEP results.

Finally, we evaluate the importance of variational optimization of the dividing surface. Conventional TST places a dividing surface orthogonal to the MEP passing through the saddle point, which in a classical world would yield an upper bound to the rate constant. We can evaluate the importance of variational placement of the dividing surface to minimize the classical rate constant by comparing the conventional TST rate constant [i.e., the rate constant determined with $s = 0$ in Eq. (1)] to the CVT rate constant [i.e., the rate constant determined with $s = s_*^{\text{CVT}}$ in Eq. (1)]. At all temperatures for both H and D on moving Cu(100) with N_p = 56, the conventional TST rate constant is exactly equal to the CVT rate constant, indicating that variational optimization of the dividing surface is not important for these systems. For the rigid (N_p = 0) system, variational optimization makes a slight difference in the calculated rate

constants. The effects are greater at lower temperatures and are greater for H than for D. Specifically, variational optimization decreases the H/Cu diffusion coefficient by 34% and 5% at 40 K and 1000 K, respectively. The D/Cu diffusion coefficient is decreased by 8% and 4% at these temperatures upon variational optimization.

3.2. H/Ni(100)

For a system with only one non-metal atom, the total potential energy is estimated by the embedded atom method (EAM)[96,97] as

$$V = \sum_i \left[F_i(\overline{\rho}_i) + \tfrac{1}{2} \sum_{j \neq i} \phi_{ij}(R_{ij}) \right]. \tag{33}$$

In this expression, the summations over i and j are over all atoms in the system, $F_i(\overline{\rho}_i)$ is the energy required to embed atom i into a vacancy at a point where the electron density due to all other atoms in the system is $\overline{\rho}_i$, ϕ_{ij} is a pair potential, and R_{ij} is the internuclear distance between atoms i and j. The expressions for the electron densities are given in other references.[93,96]

The energy to embed a hydrogen atom at a point where the density is ρ is given by[98]

$$F_{\mathrm{H}}(\rho) = \alpha_{\mathrm{H}} \rho \exp(-\beta_{\mathrm{H}} \rho) \tag{34}$$

and that to embed a nickel atom is given by[98]

$$F_{\mathrm{Ni}}(\rho) = \begin{cases} A\rho\exp(-\alpha\rho) + B\rho^3\exp(-\beta\rho) + C\rho\exp(-\gamma\rho), & 0 \le \rho \le \rho_c - \Delta \\ A_s(\rho-\rho_c)^5 + B_s(\rho-\rho_c)^4 + C_s(\rho-\rho_c)^3 + D_s, & \rho_c - \Delta < \rho \le \rho_c \\ D_s, & \rho_c < \rho \end{cases} \tag{35}$$

where the coefficients have been adjusted for the present work to agree as closely as possible with experimental results as discussed below. The repulsive pair potential, ϕ_{ij}, is defined as

$$\phi_{ij}(R_{ij}) = \frac{C Z_i(R_{ij}) Z_j(R_{ij})}{R_{ij}} \tag{36}$$

where C is a constant, and $Z(R_{ij})$ is the effective charge for the atom defined by Foiles *et al.*, as[99]

$$Z(R_{ij}) = Z_0\left(1 + \beta R^{\gamma}\right)\exp(-\alpha R) \tag{37}$$

where the parameters Z_0, α, β, and γ have again been determined to match experiment. The cutoffs for the electron density contributions and the pair potential are established by a smoothing function which has been defined previously.[100]

The work presented here used EAM parameter set 5 (EAM5). For a complete description of and discussion of the evolution of this parameter set, see reference 93. For the Ni(100) surface, EAM5 accurately reproduces experimental hydrogen vibrational frequencies and surface binding energies. Table 7 lists the surface binding energies, hydrogen-nickel equilibrium interatomic distances, hydrogen distances above the surface plane, and hydrogen vibrational frequencies calculated by EAM5 and compares them to literature values quantities.[38,101–111] The EAM5 potential also accurately reproduces the bulk values[112–116] of the monovacancy formation energy (E_{1V}^F) and the sublimation energy (E_S). The energetically minimized bulk lattice constant, R_0, for EAM5 is 3.5211 Å, fit to the experimental value of 3.52 Å.[92] These three bulk quantities are compared to experiment in Table 8.

Ni, like Cu, crystallizes as an FCC structure, and the picture in Figure 1 applies here as well as to Cu. Diffusion coefficients for H on Ni(100) at the CVT, CVT/SCT, and CVT/SCTQ levels are given in Table 9 for the rigid ($N_p = 0$) and moving ($N_p = 36$) Ni(100) surfaces.

As for Cu(100), the CVT/SCTQ diffusion coefficients for Ni(100) level off at low T and become independent of temperature. Figure 6 is an Arrhenius plot of the CVT/SCTQ diffusion coefficients. The plot also shows experimental results performed at a variety of surface coverages varying from $\theta = 0.12$ to 1.0 and the results of one other theoretical study. George *et al.*[50] and Mullins *et al.*[57] measured the diffusion coefficient with laser-induced thermal desorption at several temperatures between 211 and 283 K. Lin and Gomer[49] used the field emission fluctuation technique,[41] and Zhu and co-workers[60,61] used linear optical diffraction techniques to examine this process at lower temperatures (between 75 and 200 K). Mattsson *et al.*[38] studied the process with path integral techniques with an EAM potential function and used numerical Monte Carlo techniques to evaluate the path integrals. Their study covered a temperature range down to 25 K, but to preserve the resolution of the Arrhenius plot and enable adequate visual comparison to other results, only results down to 40 K are shown in Figure 6.

Diffusion coefficients are plotted for the George *et al.*,[50] Mullins *et al.*,[57] and Zhu *et al.*[60] experiments and for the calculations of Mattsson *et al.*.[38] For the Lee *et al.*[61] experiments, the data were fit to an Arrhenius form,

$$D(T) = D_0 \exp\left(\frac{-E_a}{RT}\right) \tag{38}$$

where R is the gas constant, and E_a is the activation energy, which can be determined from Eq. (38) as

$$E_a(T) = -R\frac{d\{\ln[D(T)]\}}{d(1/T)}. \tag{39}$$

Table 7. Binding energies (kcal/mol), hydrogen-nickel interatomic distance (Å), hydrogen height above the surface (Å), and hydrogen vibrational frequencies (cm^{-1}) calculated in this study [for a rigid ($N_p = 0$) and moving ($N_p = 36$) Ni(100) surface] compared to experimental and calculated values from the literature. In the literature column, experimental values are listed first, followed by calculated values in parentheses.

	Binding energy			$R_{H\text{-}Ni}$			$R_{H\text{-surface}}$			Frequencies		
Site	$N_p = 0$	$N_p = 36$	Lit.	$N_p = 0$	$N_p = 36$	Lit.	$N_p = 0$	$N_p = 36$	Lit.	$N_p = 0$	$N_p = 36$	Lit.
H(a)	64.73	64.76	64.4 ± 0.6[a]	1.84	1.83	1.82–1.84[b]	0.53	0.50	0.5 ± 0.1[b]	767	753	589[c]
			64.6 ± 0.9[d]			1.9–2.0[e]			0.9–1.0[e]			597[a]
			(62)[f]			(1.78)[g]			(0.3)[g]			621[h]
			(62)[i]			(1.8)[j]			(0.32)[j]			(532)[k]
			(69)[g]			(1.91)[f]			(0.8)[i]			(588)[g]
			(79)[j]			(1.92)[i]						(613)[f]
												(637)[i]
												(686)[l]
												(726)[j]
										517	524	387[c]
												(645)[g]
‡a	60.73	60.76	(63)[g]	1.56	1.56		0.94	0.93		1277	1270	(1428)[g]
			(77)[j]							438	449	
										290i	292i	

[a]Christmann, Schober, Ertl, and Neumann, Ref. 102

[b]Stensgaard and Jakobsen (D/Ni), Ref. 108

[c]Mårtensson, Nyberg, and Andersson, Ref. 111

[d]Lapujoulade and Neil, Ref. 101

[e]Rieder and Wilsch, Ref. 106

[f]Nordlander, Holloway, and Nørskov, Ref. 107

[g]Upton and Goddard, Ref. 104

[h]Anderson, Ref. 103

[i]Nørskov, Ref. 105

[j]Umrigar and Wilkins, Ref. 109

[k]Karlsson, Mårtensson, Andersson, and Nordlander, Ref. 110

[l]Mattsson, Engberg, and Wahnström, Ref. 38

Table 8. EAM5 calculated values for bulk lattice quantities compared to experiment.

Quantity	EAM5	experiment
monovacancy formation energy	1.66 eV	1.39–1.70 eV[a]
sublimation energy	4.43 eV	4.45 eV[b]
bulk lattice constant	3.5211 Å	3.52 Å[c]

[a] Refs. 112–115

[b] Ref. 116

[c] Ref. 92

Table 9. CVT, CVT/SCT, and CVT/SCQT diffusion coefficients (cm^2/s) for H on rigid ($N_p = 0$) and moving ($N_p = 36$) Ni(100) surfaces at a variety of temperatures. Numbers in parentheses are powers of 10.

	$N_p = 0$			$N_p = 36$		
T (K)	CVT	CVT/SCT	CVT/SCQT	CVT	CVT/SCT	CVT/SCQT
40	3.43(-25)	2.67(-15)	1.88(-14)	3.01(-25)	2.59(-15)	1.83(-14)
50	7.38(-21)	5.29(-15)	1.92(-14)	6.68(-21)	5.24(-15)	1.88(-14)
60	5.89(-18)	1.31(-14)	2.39(-14)	5.47(-18)	1.31(-14)	2.36(-14)
80	2.67(-14)	3.41(-13)	3.41(-13)	2.54(-14)	3.44(-13)	3.49(-13)
100	4.37(-12)	1.55(-11)	1.21(-11)	4.26(-12)	1.55(-11)	1.26(-11)
120	1.35(-10)	3.01(-10)	2.03(-10)	1.34(-10)	3.02(-10)	2.12(-10)
200	1.49(-7)	1.92(-7)	1.35(-7)	1.51(-7)	1.97(-7)	1.40(-7)
250	1.28(-6)	1.50(-6)	1.14(-6)	1.31(-6)	1.54(-6)	1.17(-6)
300	5.43(-6)	6.08(-6)	4.85(-6)	5.58(-6)	6.25(-6)	5.01(-6)
400	3.35(-5)	3.57(-5)	3.04(-5)	3.46(-5)	3.67(-5)	3.13(-5)
500	9.97(-5)	1.04(-4)	9.16(-5)	1.03(-4)	1.07(-4)	9.47(-5)
600	2.06(-4)	2.11(-4)	1.91(-4)	2.12(-4)	2.19(-4)	1.98(-4)
800	5.04(-4)	5.12(-4)	4.76(-4)	5.22(-4)	5.30(-4)	4.93(-4)
1000	8.59(-4)	8.68(-4)	8.20(-4)	8.90(-4)	8.99(-4)	8.49(-4)

Then Eq. (38) yields the pre-exponential factor, $D_0(T)$. Notice that both $E_a(T)$ and $D_0(T)$ are treated as functions of temperature. The two-part linear plot for this data in Figure 6 is derived from the pre-exponential factors and activation energies in two temperature ranges (120–160 K and 160–200 K for hydrogen, and 120–170 K and 170–200 K for deuterium) reported in Ref. 61. For the Lin and Gomer[49] experiments, the data in the high-temperature region of the plot in Figure 6 is derived from the pre-exponential factor and activation energy of the data in that region, and the data in the low-temperature region is estimated from the fit for this data in Ref. 49. The current results are calculated in the low-coverage single-adatom limit.

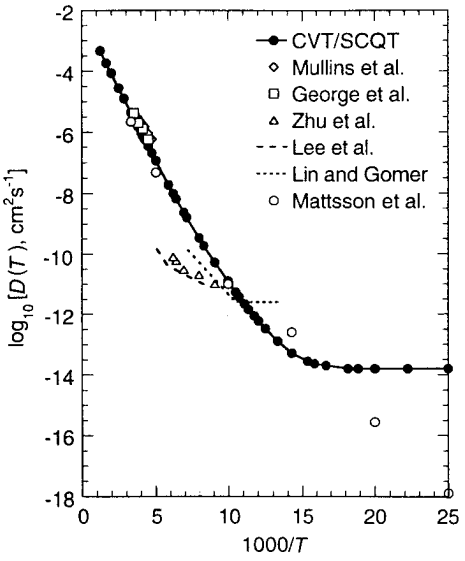

Figure 6. Arrhenius plot for H diffusion on Ni(100) compared to experimental measurements and theoretical calculations.

Our results are in excellent agreement with those of George *et al.*[50] and Mullins *et al.*[57] and with the high-temperature results of Mattsson *et al.*,[38] and they are in reasonable agreement with those of Lin and Gomer.[49] All low-temperature measurements and calculations (i.e., all except the Mullins *et al.*,[57] and George *et al.*[50] experiments) showed a leveling off of the Arrhenius plot similar to that which was discussed in the previous section for H on Cu(100).

Lin and Gomer[49] find the transition temperature to occur at about 100 K, and Zhu and co-workers[60,61] find it to occur at approximately 160 K. The results of the path integral studies by Mattsson *et al.*[38] showed the transition temperature to occur at about 40 K, somewhat low in comparison to experiment, and this transition temperature is not shown in Figure 6. Using Eq. (31) and a parabolic fit to the V_a^{AG} curve as a function of s in mass-scaled coordinates with μ = 1 amu from $s = -1.2$ Å to s = 1.2 Å, where $s^R \approx -1.5$ Å, we calculate $\left|\overline{v}^{\ddagger}\right|$ for this process to be 288 cm^{-1}. Using this value with Eq. (28) yields a transition temperature, T_{tr} = 66 K, which is, to our knowledge, the only theoretical approximation to predict a transition temperature so close to the experimentally reported values.

We note that computing $\left|\overline{v}^{\ddagger}\right|$ from the second derivative of $V_{MEP}(s)$ at its maximum instead of from a global fit to $V_a^G(s)$ would have yielded 292 cm^{-1} (see Table 7), resulting in the same level of agreement.

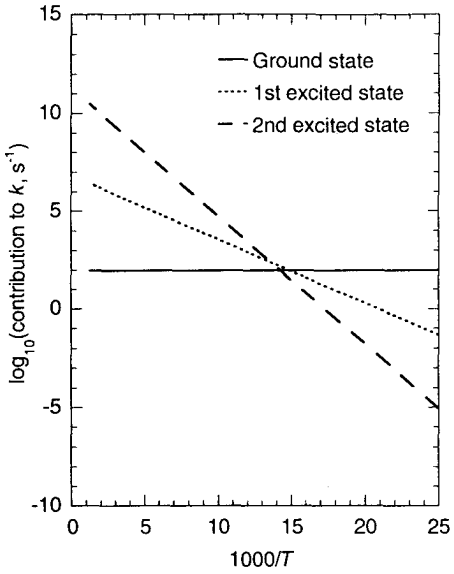

Figure 7. Logarithm to the base 10 of contributions to the rate constant of each quantized state with energy below V_a^{AG} versus inverse temperature for H diffusion on Ni(100) with $N_p = 36$.

We analyze the level-off regime by examining the individual contributions to the rate constant of each of the quantized states below V_a^{AG} as we did with the Cu(100) studies. In Figure 7, the logarithm of the contributions to the rate constant of each of the quantized states is plotted against the same abscissa used in the Arrhenius plot in Figure 6. Again we find that the onset of visual temperature independence on the Arrhenius plot coincides with the temperature at which the ground-state contribution to the rate constant is greater than the first excited state contribution to the rate constant by about one order of magnitude. Lin and Gomer[49] find the level-off temperature to coincide with the transition temperature at about 100 K. Zhu and co-workers[60,61] do not observe a level-off temperature in their experiments. They present results for the diffusion coefficient measured at temperatures as low as 120 K, at which point the diffusion coefficient is still not visually temperature independent, therefore we can only state that the level-off temperature in these experiments is below 120 K. Mattsson *et al.*[38] found the level-off temperature to coincide with the transition temperature at 40 K. For this process, we calculate $\overline{\upsilon}_3^R = 524$ cm^{-1} with the EAM5 potential surface. Using Eq. (31) with this quantity and $\left|\overline{\upsilon}^{\ddagger}\right|$ given above yields a level-off temperature of $T_0 = 55$ K. This temperature is consistent with the Arrhenius plot, justifying the model of Eq. (31) for this process.

We also make one very important remark about these results in terms of Eq. (20). Lin and Gomer[49] and Zhu and co-workers[60,61] suggest that the transition temperature marks a shift from activated over-barrier diffusion to non-activated tunneling diffusion. This hypothesis is based on the observation that at the transition temperature, the activation energy shifts dramatically from a high value, which is close to the assumed classical barrier height of the reaction, to a much lower value, indicating that at this temperature, tunneling begins to dominate the reaction. To determine whether this is an accurate interpretation of the transition temperature, we calculated $k_{\mathrm{tun}}(T)$ from Eq. (25) [M = 2 for H diffusion on Ni(100)] where the energy eigenstates, E_0^{R}, E_1^{R}, and E_2^{R}, were determined by Eq. (12) ($\overline{\upsilon}_3^{\mathrm{R}}$ = 524 cm^{-1} for this process with N_p = 36 as mentioned above), and the transmission probabilities, $P^{\mathrm{G}}\left(E_v^{\mathrm{R}}\right)$, were calculated in the SCTQ approximation as 1.87 x 10^{-12}, 1.36 x 10^{-7}, and 3.06 x 10^{-3}, for v = 0, 1, and 2, respectively. At the transition temperature, T_{tr} = 66 K, k_{tun} is equal to 2.44 x 10^2, and $k_{\mathrm{tun}}(T_{\mathrm{tr}})+k_{\mathrm{over}}(T_{\mathrm{tr}})$ is equal to 2.51 x 10^2, which yields $F_{\mathrm{tun}}(T_{\mathrm{tr}})$ = 0.97 from Eq. (20). This indicates that at the transition temperature, 97% of the process still occurs by a tunneling mechanism. Similar calculations at temperatures above T_{tr} indicate that tunneling still dominates well above the transition temperature. For example, the tunneling contributes about 55% of the hops when T = 125 K. Therefore, we conclude that the transition temperature does not mark the shift from over-barrier activated diffusion to tunneling diffusion, but rather it indicates the point at which excited-state contribution to the rate constant becomes negligible compared to the ground-state contribution.

The data in Figure 6 are fit to an Arrhenius form, Eqs. (38) and (39), and the pre-exponential factors and activation energies for various temperature ranges are extracted from the plot and compared to experiment in Table 10. As expected, our activation energies and pre-exponential factors agree very well with those of Mullins *et al.*[57] and of George *et al.*[50] in the temperature ranges of those experiments. Only below the transition temperatures of the other low-temperature experiments do our calculations disagree significantly with any of the experimental values. This is, of course, simply an artifact of various locations of the transition temperature. That is, since our calculated transition temperature is lower than the experimental ones, our low-temperature diffusion coefficients are also lower than experiment, because our diffusion coefficients continue to decrease after the experimental ones have leveled off.

Finally, we note that variational optimization of the dividing surface is not important for the H/Ni(100) surface diffusion process. For all temperatures studied and for both N_p = 0 and N_p = 36, we find s_*^{CVT} = 0, so the CVT rate constant is precisely equal to the conventional TST rate constant.

Table 10. Activation energies (E_a, kcal/mol) and pre-exponential factors (D_0, cm^2/s) for surface diffusion of H on Ni(100) with 36 moving Ni atoms for several temperature ranges compared to experimental values. Powers of 10 in parentheses.

	E_a		D_0	
T(K)	CVT/SCTQ	Experiment	CVT/SCTQ	Experiment
40–50	0.011		2.09 (-14)	
55–65	0.41		8.36 (-13)	
70–80	1.9		6.79 (-8)	
85–95	2.9		2.64 (-5)	
100–140	3.5	3.2[a]	5.33 (-4)	8. (-6)[a]
120–170	3.8	1.2[b]	1.66 (-3)	1.5 (-9)[b]
156–161	3.9	3.5[c]	2.69 (-3)	8. (-6)[c]
170–200	4.1	3.5[b]	4.28 (-3)	1.1 (-6)[b]
211–263	4.3	3.5 ± 0.3[d]	6.17 (-3)	2.5 (-3)[d]
223–283	4.3	4 ± 0.5[e]	6.55 (-3)	4.5 (-3)[e]
300–400	4.4		7.64 (-3)	

[a]Lin and Gomer, Ref. 49

[b]Lee, Zhu, Deng, and Linke, Ref. 61

[c]Zhu, Lee, Wong, and Linke, Ref. 60

[d]Mullins, Roop, Costello, and White, Ref. 57

[e]George, DeSantolo, and Hall, Ref. 50

4. CONCLUDING REMARKS

In this chapter, we reviewed canonical variational transition state theory with the small-curvature tunneling approximation with quantized reactant states. We presented results obtained by such calculations for the diffusion of H and D on Cu(100) and for diffusion of H on Ni(100). Where applicable, we compared the calculated diffusion coefficients to experimental values and to other theoretical calculations, and in most cases we found very close agreement. We showed that at very low temperatures, the diffusion coefficient loses its temperature dependence for both interfaces, and this is in agreement with three sets of experimental results on the Ni(100) surface. We showed that this onset of temperature independence occurs when the ground-state contribution to the diffusion coefficient is greater than that of the first excited state by about one order of magnitude.

We also showed that the EAM5 embedded atom parameter set for the H on Ni system gives very good agreement with experimentally determined energetics, H-Ni interatomic distances, and vibrational frequencies for the (100) surface as well as with quantities defining

the lattice itself (monovacancy formation energy, sublimation energy, and bulk lattice constant). Current and future work is being aimed at fitting a new embedded atom parameter set so that these experimental quantities are also accurately reproduced for the Ni(111) crystal face without damaging current agreement with the (100) face and bulk quantities. An accurate potential energy surface for the H/Ni system (gas-solid interface and bulk) will allow us to study subsurface processes[117] and eventually to carry out calculations for other reactions such as the Ni(111) surface catalyzed reaction of H with methyl radical.

ACKNOWLEDGMENTS

This work was supported in part by the National Science Foundation through grant no. CHE89-22048.

REFERENCES

1. C.N. Satterfield, "Heterogeneous Catalysis in Practice," McGraw-Hill, New York (1980).
2. G. Somorjai, "Chemistry in Two Dimensions," Cornell University, New York (1981).
3. G.C. Bond, "Heterogeneous Catalysis," 2nd ed., Oxford University, Oxford (1987).
4. I.M. Campbell, "Catalysis at Surfaces," Chapman and Hall, Ltd., New York (1988).
5. R.A. van Santen, "Theoretical Heterogeneous Catalysis," World Scientific, Singapore (1991).
6. F. Ruette, ed., "Quantum Chemistry Approaches to Chemisorption and Heterogeneous Catalysis," Kluwer, Dordrecht (1992).
7. V.T. Binh, ed., "Surface Mobilities on Solid Materials," Plenum, New York (1983).
8. M. Boudart and G. Djéga-Mariadassou, "Kinetics of Heterogeneous Catalytic Reactions," Princeton University, Princeton, NJ (1984).
9. E. Shustorovich, ed., "Metal-Surface Reaction Energetics," VCH, New York (1991).
10. M.G. Lagally, Atom motion on surfaces, *Physics Today,* November 1993: 24.
11. K. Kitahara, H. Metiu, J. Ross, and R. Sibley, *J. Chem. Phys.* 65: 2871 (1976).
12. S. Efrima and H. Metiu, *J. Chem. Phys.* 69: 2286 (1978).
13. S. Efrima and H. Metiu, *J. Chem. Phys.* 69: 5113 (1978).
14. K. Haug, G. Wahnström, and H. Metiu, *J. Chem. Phys.* 92: 1083 (1990).
15. K. Haug and H. Metiu, *J. Chem. Phys.* 94: 3251 (1991).
16. J.P. Sethna, *Phys. Rev. B* 24: 698 (1981).
17. K.A. Muttalib and J. Sethna, *Phys. Rev. B* 32: 3462 (1985).
18. S.M. Valone, A.F. Voter, and J.D. Doll, *Surf. Sci.* 155: 687 (1985).
19. S.M. Valone, A.F. Voter, and J.D. Doll, *J. Chem. Phys.* 85: 7480 (1986).
20. J.D. Doll and A.F. Voter, *Annu. Rev. Phys. Chem.* 38: 413 (1987).
21. S.W. Rick, D.L. Lynch, and J.D. Doll, *J. Chem. Phys.* 99: 8183 (1993).
22. J.G. Lauderdale and D.G. Truhlar, *J. Amer. Chem. Soc.* 107: 4590 (1985).

23. J.G. Lauderdale and D.G. Truhlar, *Surf. Sci.* 164: 558 (1985).

24. J.G. Lauderdale and D.G Truhlar, *J. Chem. Phys.* 84: 1843 (1986).

25. T.N. Truong and D.G. Truhlar, *J. Phys. Chem.* 91: 6229 (1987).

26. T.N. Truong and D.G. Truhlar, *J. Chem. Phys.* 88: 6611 (1988).

27. T.N. Truong, D.G. Truhlar, J.R. Chelikowsky, and M.Y. Chou, *J. Phys. Chem.* 94: 1973 (1990).

28. T.N. Truong and D.G. Truhlar, *J. Chem. Phys.* 93: 2125 (1990).

29. S.E. Wonchoba and D.G. Truhlar, *J. Chem. Phys.* 99: 9637 (1993).

30. R. Jaquet and W.H. Miller, *J. Phys. Chem.* 89: 2139 (1985).

31. K.F. Freed, *J. Chem. Phys.* 82: 5264 (1985).

32. (a) A. Auerbach, K. F. Freed, and R. Gomer, *J. Chem. Phys.* 86: 2356 (1987); (b) M.D. Miller, *Surf. Sci.* 127: 383 (1983); (c) Q. Niu, *J. Stat. Phys.* 65: 317 (1991); (d) R. Nieminen, *Nature* 356: 289 (1992).

33. R.M. Stratt, *Phys. Rev. Lett.* 55: 1443 (1985).

34. K.B. Whaley, A.N. Nitzan, and R.B. Gerber, *J. Chem. Phys.* 84: 5181 (1986).

35. P.D. Reilly, R.A. Harris, and K.B. Whaley, *J. Chem. Phys.* 97: 6875 (1992).

36. B.M. Rice, B.C. Garrett, M.L. Koszykowski, S.M. Foiles, and M.S. Daw, *J.Chem. Phys.* 92: 775 (1990).

37. Y.-C. Sun and G.A. Voth, *J. Chem. Phys.* 98: 7451 (1993).

38. T. R. Mattsson, U. Engberg, and G. Wahnström, *Phys. Rev. Lett.* 71: 2615 (1993).

39. R. Wortman, R. Gomer, and R. Lundy, *J. Chem. Phys.* 27: 1099 (1957).

40. R. DiFoggio and R. Gomer, *Phys. Rev. Lett.* 44: 1258 (1980).

41. G. Mazenko, J.R. Banavar, and R. Gomer, *Surf. Sci.* 107: 459 (1981).

42. R. DiFoggio and R. Gomer, *Phys. Rev. B* 25: 3490 (1982).

43. R. Gomer, *Comments on Solid State Phys.* 10: 253 (1983).

44. R. Gomer, *Vacuum* 33: 537 (1983).

45. R. Gomer, *in:* "Dynamics on Surfaces," B. Pullman, J. Jortner, A. Nitzan, and B. Gerber, eds., Reidel, Dordrecht (1984), p. 203.

46. C. Dharmadhikari and R. Gomer, *Surf. Sci.* 143: 223 (1984).

47. S.C. Wang and R. Gomer, *J. Chem. Phys.* 83: 4193 (1985).

48. E.A. Daniels, J.C. Lin, and R. Gomer, *Surf. Sci.* 204: 129 (1988).

49. T.-S. Lin and R. Gomer, *Surf. Sci.* 255: 41 (1991).

50. S.M. George, A.M. DeSantolo, and R.B. Hall, *Surf. Sci.* 159: L425 (1985).

51. (a) C. H. Mak, J.L. Brand, A.A. Deckert, and S.M. George, *J. Chem. Phys.* 85: 1676 (1986); (b) C. H. Mak, J.L. Brand, B.G. Koehler, and S.M. George, *Surf. Sci.* 188: 312 (1987); (c) C. H. Mak, J.L. Brand, B.G. Koehler, and S.M. George, *Surf. Sci.* 191: 108 (1987); (d) C. H. Mak, J.L. Brand, B.G. Koehler, and S.M. George, *J. Chem. Phys.* 87: 2340 (1987); (e) J.L. Brand, A.A. Deckert, and S.M. George, *Surf. Sci.* 194: 457 (1988); (f) C. H. Mak, A.A. Deckert, and S.M. George, *J. Chem. Phys.* 89: 5242 (1988); (g) C. H. Mak, and S.M. George, *Chem. Phys. Lett.* 135: 381 (1987); (h) A.A. Deckert, J.L. Brand, M.V. Arena, and S.M. George, *J. Vac. Sci. Technol.* A6: 794 (1988); (i) A.A. Deckert, J.L. Brand, M.V. Arena, and S.M. George, *Surf. Sci.* 208: 441 (1989); (j) C. H. Mak, B.G. Koehler, and S.M. George, *J. Vac. Sci. Technol.* A6: 856 (1988); (k) J.L. Brand, A.A. Deckert, M.V.

Arena, and S.M. George, *J. Phys. Chem.* 92: 5136 (1990); (l) E.D. Werste, M.V. Arena, A.A. Deckert, and S.M. George, *Surf. Sci.* 233: 293 (1990); (m) M.V. Arena, A.A. Deckert, J.L. Brand, and S.M. George, *J. Phys. Chem.* 94: 6792 (1990).

52. R. Viswanathan, D.R. Burgess, J.P.C. Stair, and E. Weitz, *J. Vac. Sci. Technol.* 20: 605 (1982).
53. (a) D.R. Mullins, B. Roop, and J.M. White, *Chem. Phys. Lett.* 129: 511 (1986); (b) B. Roop, S.A. Costello, D.R. Mullins, and J.M. White, *J. Chem. Phys.* 86: 3003 (1987).
54. S.M. George, *in:* "Physical Methods of Chemistry," 2nd Ed., Vol. 9A, B.W. Rossiter and R.C. Baetzold, eds., John Wiley and Sons, New York (1993), p. 474.
55. E.G. Seebauer and L.D. Schmidt, *Chem. Phys. Lett.* 123: 129 (1986).
56. E.G. Seebauer, A.C.F. Konig, and L.D. Schmidt, *J. Chem. Phys.* 88: 6597 (1988).
57. D.R. Mullins, B. Roop, S.A. Costello, and J.M. White, *Surf. Sci.* 186: 67 (1987).
58. C.-H. Hsu, B.E. Larson, M. El-Batanouny, C.R. Willis, and K.M. Martini, *Phys. Rev. Lett.* 66: 3164 (1991).
59. C. Astaldi, A. Bianco, S. Modesti, and E. Touatti, *Phys. Rev. Lett.* 68: 90 (1992).
60. X.D. Zhu, A. Lee, A. Wong, and U. Linke, *Phys. Rev. Lett.* 68: 1862 (1992).
61. A. Lee, X.D. Zhu, L. Deng, and U. Linke, *Phys. Rev. B* 46: 15472 (1992).
62. A. Lee, X.D. Zhu, A. Wong, L. Deng, and U. Linke, *Phys. Rev. B* 48: 11256 (1993).
63. M. Born and J.R. Oppenheimer, *Ann. Phys.* 84: 457 (1927).
64. M. Born and K. Huang, "Dynamical Theory of Crystal Lattices," Oxford University, New York (1956).
65. G.V. Chester, *Adv. Phys.* 10: 357 (1961).
66. D.G. Truhlar and B.C Garrett, *Accts. Chem. Research* 13: 440 (1980).
67. D.G. Truhlar, A.D. Isaacson, and B.C. Garrett, *in:* "Theory of Chemical Reaction Dynamics," M. Baer, ed., CRC Press, Boca Raton, FL (1985), Vol. 4, pp 65-137.
68. S.C. Tucker and D.G. Truhlar, *in:* "New Theoretical Methods for Understanding Organic Reactions," J. Bertrán and I.G. Czizmadia, eds., Kluwer, Dordrecht (1989), pp 219-346.
69. E.B. Wilson, Jr., J.C. Decius, and P.C. Cross, "Molecular Vibrations," McGraw-Hill, New York (1958), p. 14.
70. S. Glasstone, K.J. Laidler, and H. Eyring, "Theory of Rate Processes," McGraw-Hill, New York (1944).
71. D.G. Truhlar and A. Kuppermaan, *J. Chem. Phys.* 52: 3841 (1970).
72. D.G. Truhlar and A. Kuppermaan, *J. Chem. Phys.* 56: 2232 (1972).
73. J.M. Bowman, A. Kuppermaan, J.T. Adams, and D.G. Truhlar, *Chem. Phys. Lett.* 20: 229 (1973).
74. B.C. Garrett and D.G. Truhlar, *J. Chem. Phys.* 70: 1593 (1979).
75. B.C. Garrett and D.G. Truhlar, *J. Phys. Chem.* 83: 1079 (1979).
76. D.G. Truhlar, A.D. Isaacson, R.T. Skodje, and B.C. Garrett, *J. Phys. Chem.* 86: 2252 (1982).
77. D.G. Truhlar, W.L. Hase, and J.T. Hynes, *J. Phys. Chem.* 87: 2664, 5523(E) (1983).
78. B.C. Garrett, D.G. Truhlar, R.S. Grev, and A.W. Magnuson, *J. Phys. Chem.* 84: 1730 (1980).
79. J. Heading, "An Introduction to Phase Integral Methods," Methuen, London (1961).
80. B.C. Garrett and D.G. Truhlar, *J. Phys. Chem.* 83: 2921 (1979).
81. R.T. Skodje, D.G. Truhlar, and B.C. Garrett, *J. Phys. Chem.* 85: 3019 (1981).

82. R.T. Skodje, D.G. Truhlar, and B.C. Garrett, *J. Chem. Phys.* 77: 5955 (1982).

83. B.C. Garrett, D.G. Truhlar, A.F. Wagner, and T.H. Dunning, Jr. *J. Chem. Phys.* 78: 4400 (1983).

84. B.C. Garrett and D.G. Truhlar, *J. Chem. Phys.* 79: 4931 (1983).

85. B.C. Garrett, N. Abusalbi, D.J. Kouri, and D.G. Truhlar, *J. Chem. Phys.* 83: 2252 (1985).

86. D.-h. Lu, T.N. Truong, V.S. Melissas, G.L. Lynch, Y.-P. Liu, B.C. Garrett, R. Steckler, A.D. Isaacson, S.N. Rai, G.C. Hancock, J.G. Lauderdale, T. Joseph, and D.G. Truhlar, *Computer Phys. Commun.* 71: 235 (1992).

87. D.G. Truhlar, D.-h. Lu, S.C. Tucker, X. G. Zhao, A. González-Lafont, T.N. Truong, D. Maurice, Y.-P. Liu, and G.C. Lynch, *ACS Symp. Ser.* 502: 16 (1992).

88. Y.-P. Liu, G. Lynch, T.N. Truong, D.-h. Lu, D.G. Truhlar, and B.C Garrett, *J. Amer. Chem. Soc.* 115: 2408 (1993).

89. Y.-P. Liu, D.-h. Lu, A. González-Lafont, D.G. Truhlar, and B.C. Garrett, *J. Amer. Chem. Soc.* 115: 7806 (1993).

90. A.F. Voter and J.D. Doll, *J. Chem. Phys.* 80: 5832 (1984).

91. T. Halicoğlu and G.M. Pound, *Phys. Stat Solidi A* 30: 619 (1975).

92. C. Kittel, "Introduction to Solid State Physics," 6th Ed., John Wiley & Sons, New York (1986).

93. S.E. Wonchoba, W.-P. Hu, and D.G. Truhlar, to be submitted.

94. Y.-P. Liu, G.C. Lynch, W.-P. Hu, V.S. Melissas, R. Steckler, B.C. Garrett, D.-h. Lu, T.N. Truong, A.D. Isaacson, S.N. Rai, G.C. Hancock, J.G. Lauderdale, T. Joseph, and D.G. Truhlar, *QCPE Bull.* 13: 28 (1993).

95. R.T. Skodje and D.G.Truhlar, *J. Phys. Chem.* 85: 624 (1981).

96. M. Daw and M. Baskes, *Phys. Rev. B* 29: 6443 (1984).

97. M.S. Daw, S.M. Foiles, and M.I. Baskes, *Mat. Sci. Rep.* 9: 251 (1993).

98. T. N. Truong, D.G. Truhlar, and B.C. Garrett, *J. Phys. Chem* 93: 8227 (1989).

99. S.M. Foiles, M.I. Baskes, and M.S. Daw, *Phys. Rev. B* 33: 7983 (1986).

100. T.N. Truong and D.G. Truhlar, *J. Phys. Chem.* 94: 8262 (1990).

101. J. Lapujoulade and K.S. Nail, *Surf. Sci.* 35: 288 (1973).

102. K. Christmann, O. Schober, G. Ertl, and H. Neumann, *J. Chem. Phys.* 60: 4528 (1974).

103. S. Anderson, Chem. *Phys. Lett.* 55: 185 (1978).

104. T.H. Upton and W.A. Goddard, *Phys. Rev. Lett.* 42: 472 (1979).

105. J.K. Nørskov, *Phys. Rev. Lett.* 48: 1620 (1982).

106. K.H. Rieder and H. Wilsch, *Surf. Sci.* 131: 245 (1983).

107. P. Nordlander, S. Holloway, J.K. Nørskov, *Surf. Sci.* 136: 59 (1984).

108. I. Stensgaard and F. Jakobsen, *Phys. Rev. Lett.* 54: 711 (1985).

109. C. Umrigar and J.W. Wilkins, *Phys. Rev. Lett.* 54: 1551 (1985).

110. P.-A. Karlsson, A.-S. Mårtensson, S. Andersson, and P. Nordlander, *Surf. Sci.* 175: L759 (1986).

111. A.-S. Mårtensson, C. Nyberg, and S. Andersson, *Surf. Sci.* 205: 12 (1988).

112. (a) A. Seeger, D. Schumacher, W. Schilling, and J. Diehl, eds., "Vacancies and Interstitials in Metals," North Holland Pub. Co., Amsterdam (1970), p 36; (b) H. Bakker, *Phys. Stat. Solidi* 28: 569 (1968).

113. R.A. Johnson, *Phys. Rev.* 145: 423 (1965).

114. A.A. Mamalui, T.D. Ostinskaya, V.A. Pervakov, and V.I. Khomkevich, *Sov. Phys. Solid State* 10: 2290 (1969).

115. W. Wycisk, M. Feller-Kniepmeier, *J. Nucl. Mater.* 69–70: 616 (1978).

116. C.J. Smith, ed., "Metal Reference Book," 5th ed., Betterworths, London (1976), p 186.

117. K.J. Maynard, A.D. Johnson, S.P. Daley, and S.T. Ceyer, *Faraday Discuss. Chem. Soc.* 91: 437 (1991).

fcc lattice

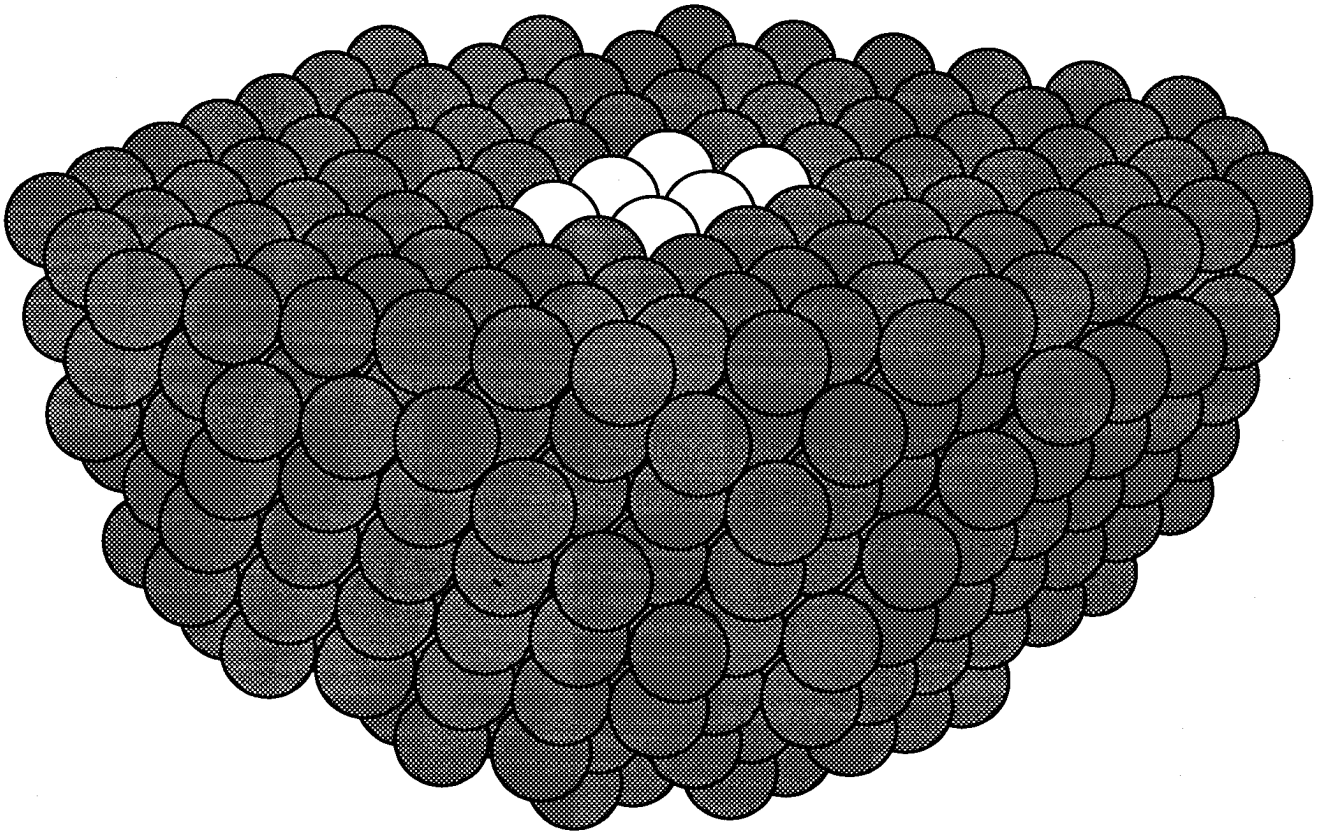

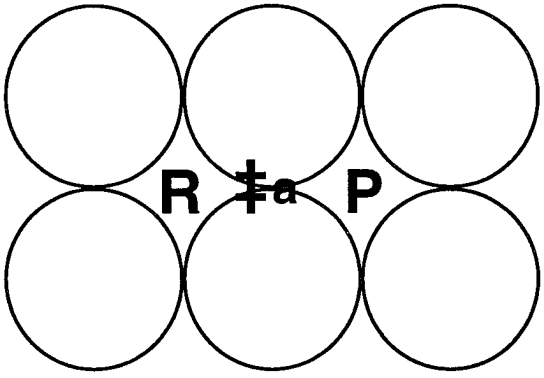

Figure 1

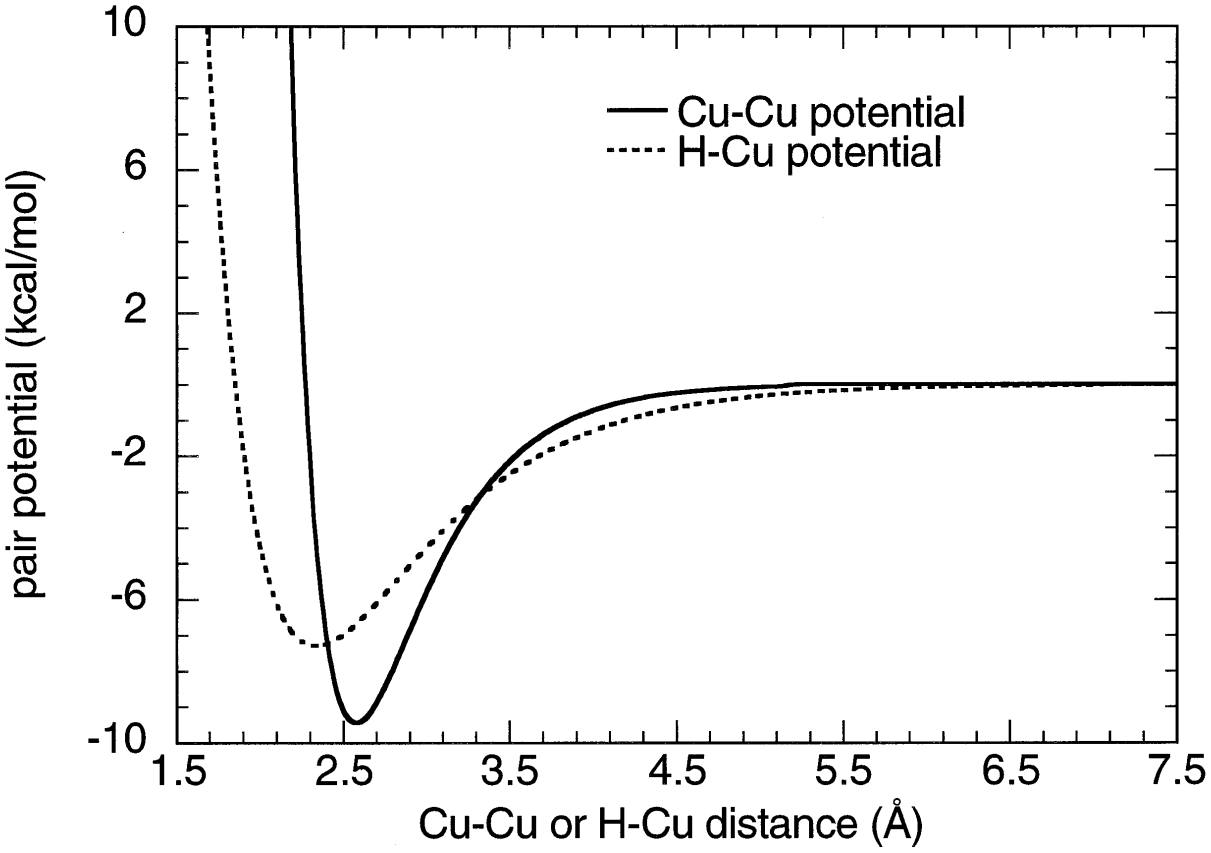
10
6
2
-2
-6
-10
pair potential (kcal/mol)
Cu-Cu potential
H-Cu potential
1.5
2.5
3.5
4.5
5.5
6.5
7.5
Cu-Cu or H-Cu distance (Å)

Figure 2

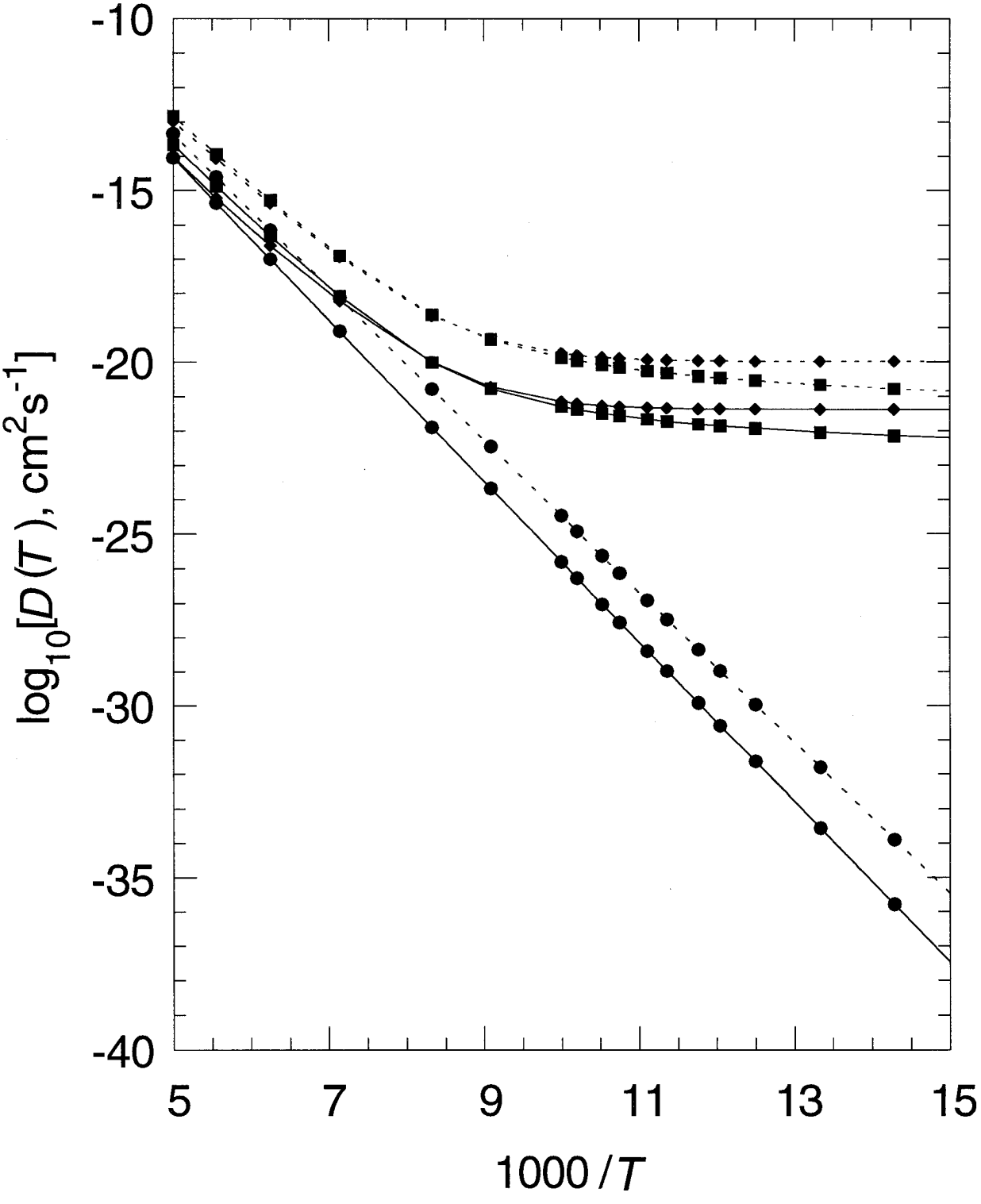

Figure 3

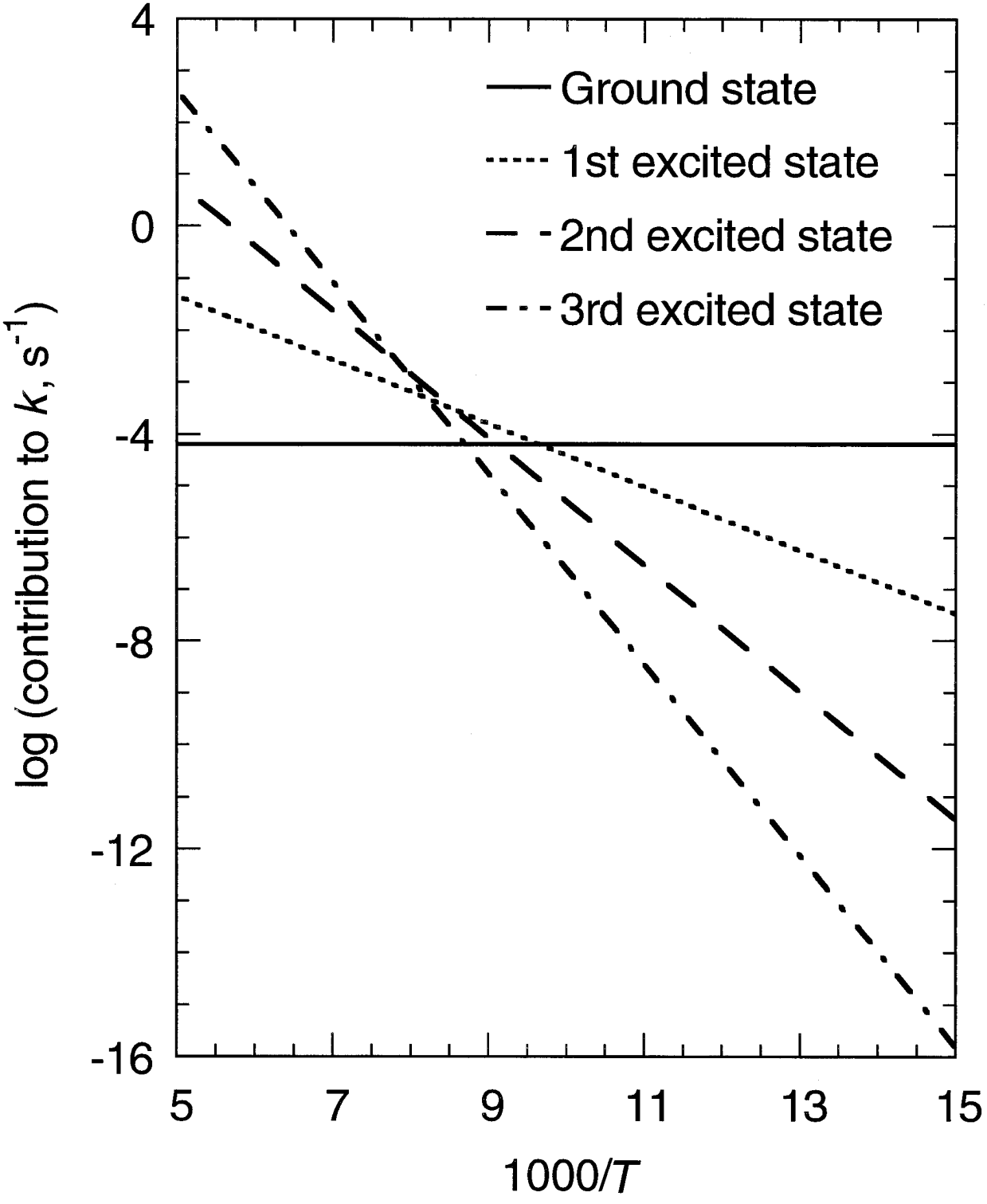
4
0
-4
-8
-12
-16
5
7
9
11
13
15
1000/T
log (contribution to k, s-1)
Ground state
1st excited state
2nd excited state
3rd excited state

Figure 4

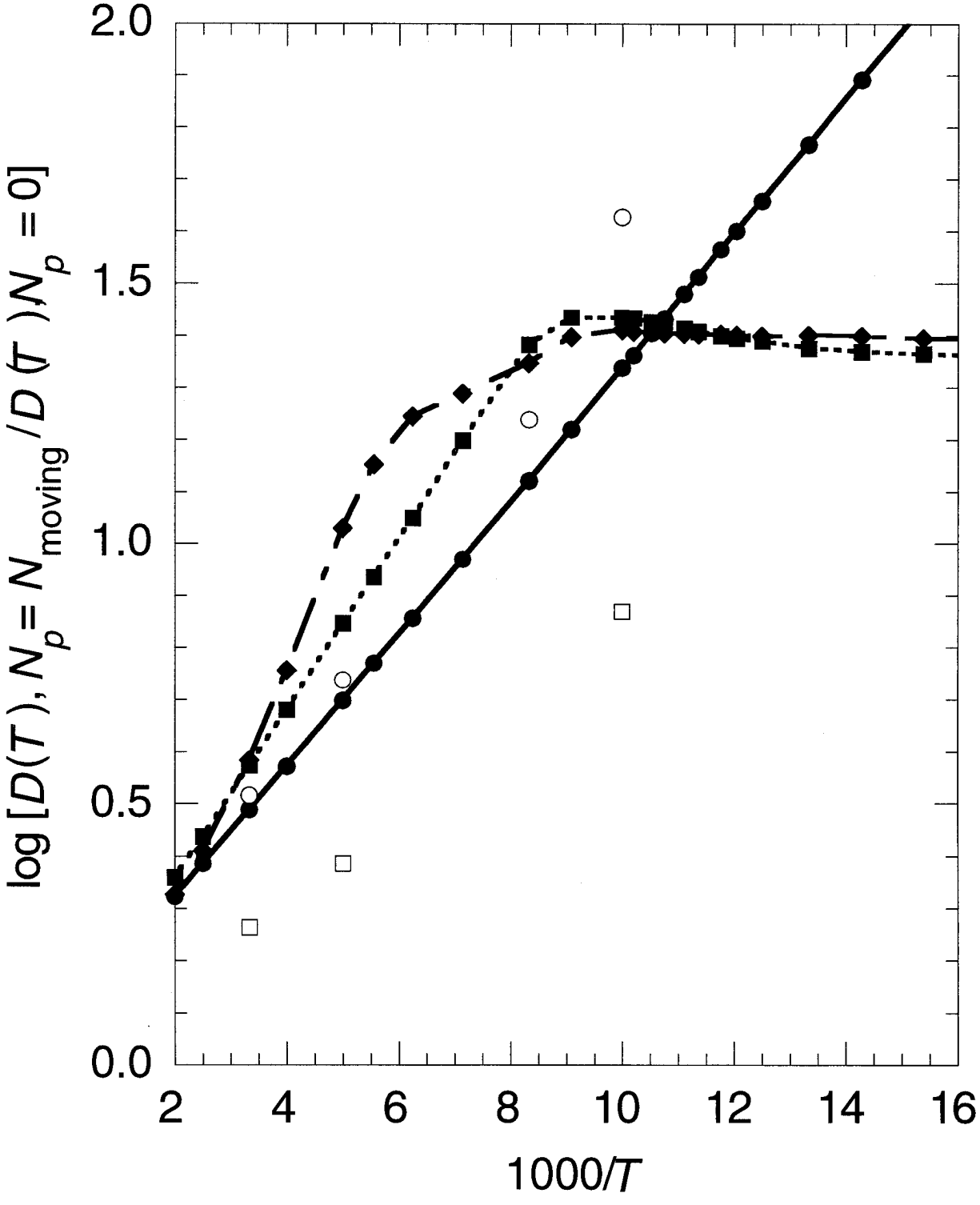

Figure 5

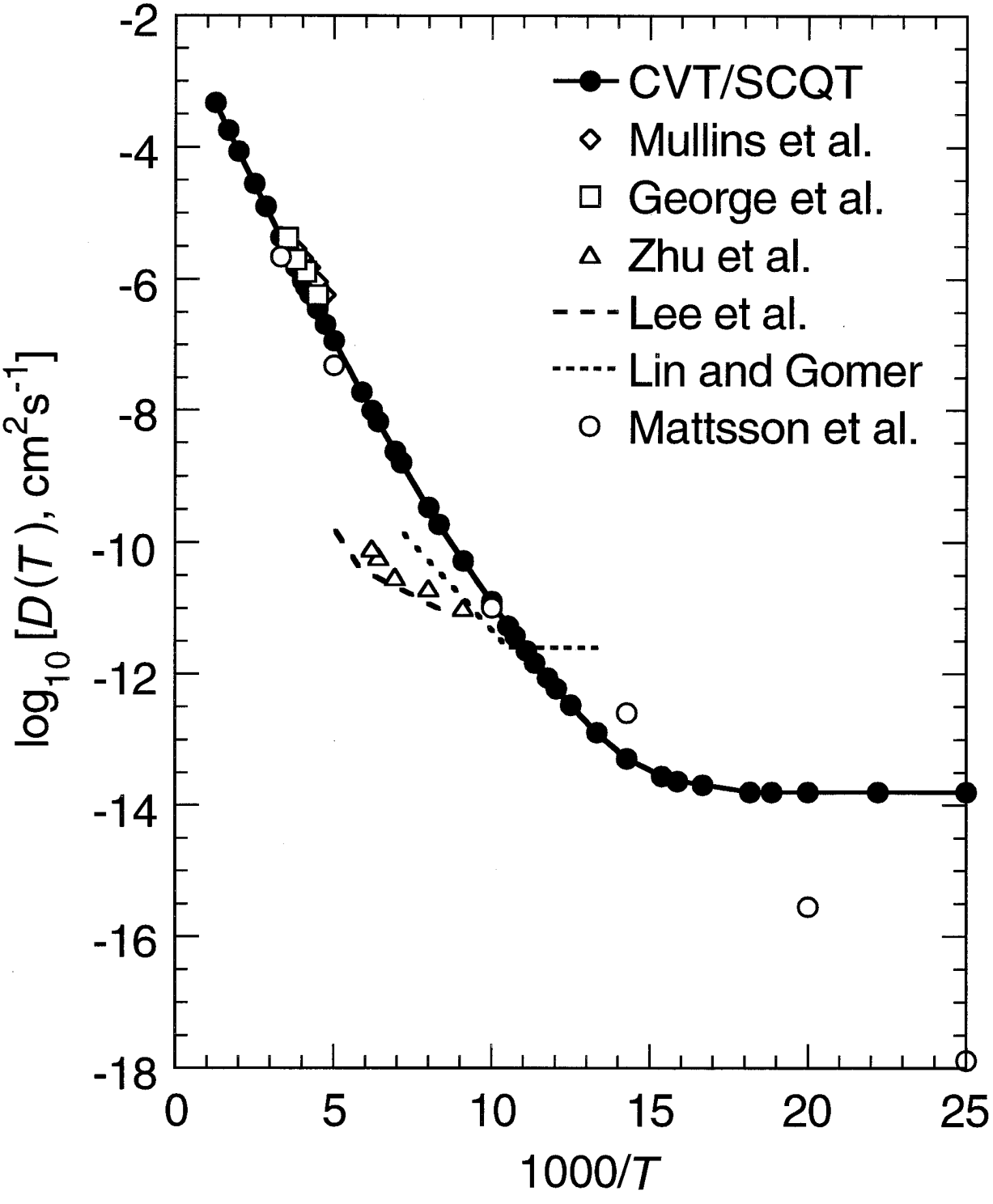
-2
-4
-6
-8
-10
-12
-14
-16
-18
0
5
10
15
20
25
1000/T
log10 [D(T), cm2s-1]
CVT/SCQT
Mullins et al.
George et al.
Zhu et al.
Lee et al.
Lin and Gomer
Mattsson et al.

Figure 6

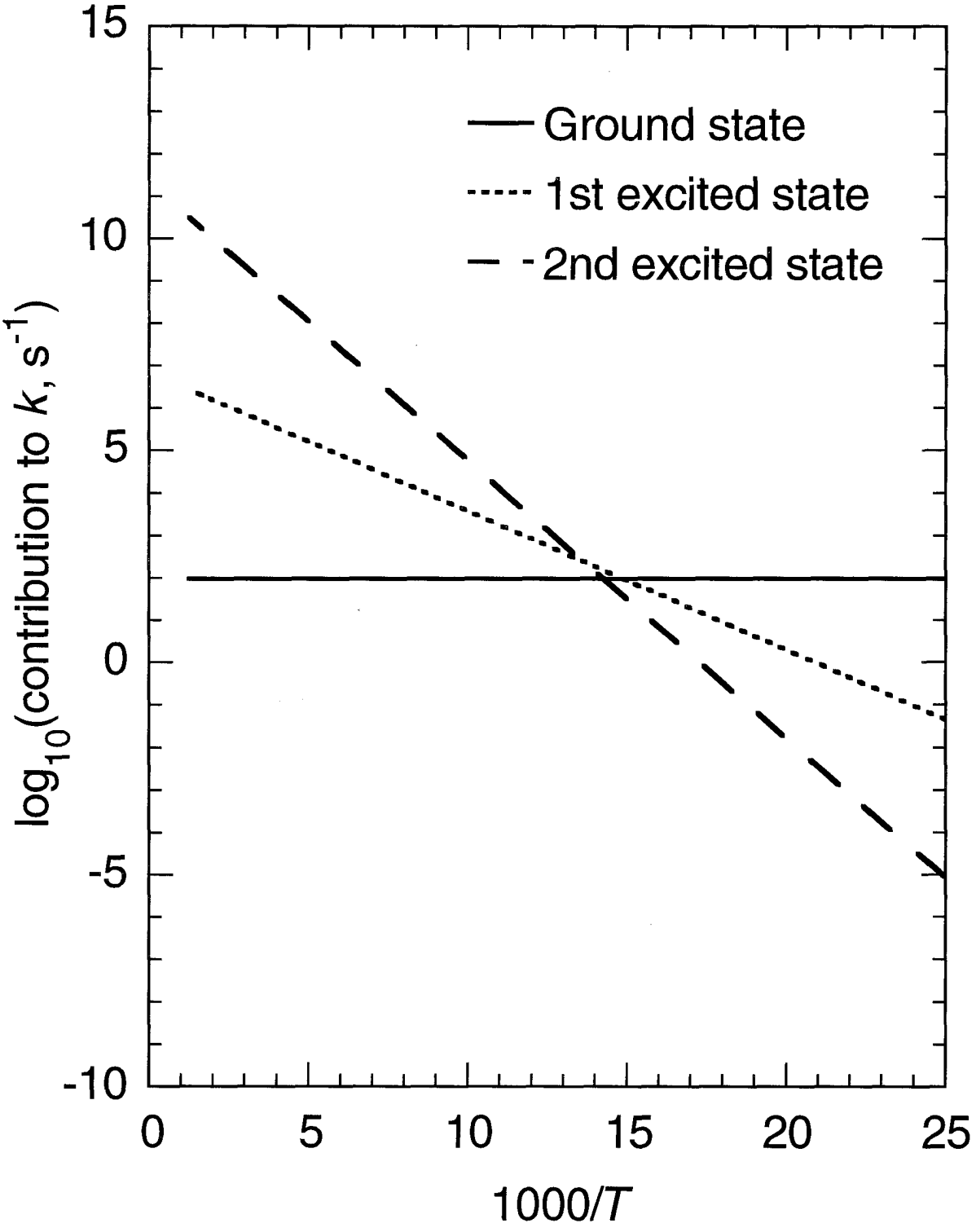
15
10
5
0
-5
-10
0
5
10
15
20
25
1000/T
log10(contribution to k, s-1)
Ground state
1st excited state
2nd excited state

Figure 7